
CITYGUARD: GRAPH-AWARE PRIVATE DESCRIPTORS FOR BIAS-RESILIENT IDENTITY SEARCH ACROSS URBAN CAMERAS

Rong Fu*
University of Macau
mc46603@um.edu.mo

Wenxin Zhang
University of the Chinese Academy of Sciences
zwxzhang12@163.com

Yibo Meng
Tsinghua University
mengyb22@mails.tsinghua.edu.cn

Jia Yee Tan
Renmin University of China
tanjiayi2002@ruc.edu.cn

Jiaxuan Lu
Shanghai AI Laboratory
lujiaxuan@pjlab.org.cn

Rui Lu
The Hong Kong University of Science and Technology
rluac@connect.ust.hk

Jiekai Wu
Juntendo University
ketsu0612@gmail.com

Zhaolu Kang
Peking University
kangz19966@gmail.com

Simon Fong
University of Macau
ccfong@um.edu.mo

February 23, 2026

ABSTRACT

City-scale person re-identification across distributed cameras must handle severe appearance changes from viewpoint, occlusion, and domain shift while complying with data protection rules that prevent sharing raw imagery. We introduce CityGuard, a topology-aware transformer for privacy-preserving identity retrieval in decentralized surveillance. The framework integrates three components. A dispersion-adaptive metric learner adjusts instance-level margins according to feature spread, increasing intra-class compactness. Spatially conditioned attention injects coarse geometry, such as GPS or deployment floor plans, into graph-based self-attention to enable projectively consistent cross-view alignment using only coarse geometric priors without requiring survey-grade calibration. Differentially private embedding maps are coupled with compact approximate indexes to support secure and cost-efficient deployment. Together these designs produce descriptors robust to viewpoint variation, occlusion, and domain shifts, and they enable a tunable balance between privacy and utility under rigorous differential-privacy accounting. Experiments on Market-1501 and additional public benchmarks, complemented by database-scale retrieval studies, show consistent gains in retrieval precision and query throughput over strong baselines, confirming the practicality of the framework for privacy-critical urban identity matching.

Keywords Privacy-preserving biometrics, geometric representation learning, graph-conditioned attention, adaptive metric learning, differential privacy, secure retrieval

1 Introduction

Person re-identification, commonly abbreviated Re-ID, concerns matching the same individual observed by different non-overlapping cameras. This task underpins many security and monitoring applications but remains challenging

*Corresponding author: mc46603@um.edu.mo

because appearance cues vary dramatically with viewpoint, illumination, occlusion, pose and clothing, all of which undermine feature consistency [1, 2, 3]. Convolutional neural networks established reliable baselines for Re-ID [3, 4] and recent advances show that vision transformers and large-scale self-supervised pretraining improve modeling of global context [5, 6, 7]. Progress in metric learning and contrastive objectives has further strengthened discrimination capabilities [8, 9, 10]. Parallel lines of work address occlusion, cross-spectral matching, temporal modeling and privacy-aware deployment [11, 12, 13, 14, 15, 16, 17].

We first clarify terminology used in this paper. By geometry we mean spatial camera properties such as three-dimensional coordinates and orientations. By topology we mean a graph structure induced from those geometric relationships; specifically, vertices represent cameras and edges encode geometric affinity or proximity. Our proposed attention mechanism operates on this topology to propagate information across physically related views.

Real-world Re-ID systems deployed at city scale must contend with heterogeneous and evolving camera sources, strict latency and throughput targets, and regulatory constraints such as GDPR and CCPA. These operational requirements create a multi-objective design problem in which accuracy, cross-view consistency and privacy preservation interact with system-level constraints. Existing approaches have notable shortcomings in this setting. Loss functions with fixed margins do not adapt to identity-specific feature dispersion across domains and therefore can harm intra-class compactness [8, 9]. Standard attention mechanisms ignore camera-layout priors and thus may fail to preserve spatial coherence across views [4, 18]. Modules that target robustness or privacy are frequently appended after model design, yielding suboptimal privacy–utility trade-offs [19, 16, 17]. Moreover, practical deployments require efficient inference, edge compatibility and privacy-aware indexing, yet few methods integrate these needs into a unified pipeline.

Motivated by these gaps, we propose *CityGuard*, a unified framework that jointly improves discrimination, encodes geometry-aware alignment and enforces privacy for identity search over distributed camera networks. *CityGuard* is built from three core components. A dispersion-aware adaptive-margin metric adjusts decision boundaries using per-identity divergence to tighten intra-class clusters. A geometry-conditioned attention module injects camera-layout priors into graph self-attention to improve cross-view alignment using only coarse geometric priors without requiring survey-grade calibration. A family of lightweight embedding transforms is calibrated for differential privacy and paired with compact approximate indexes to enable secure, low-overhead retrieval. These components are complemented by multi-scale feature extraction, graph-based temporal modeling and adversarial hardening to balance accuracy, efficiency and compliance. *CityGuard* supports tunable privacy–utility trade-offs, source-free adaptation across camera domains and scalable approximate search. The framework is applicable to tasks such as fraud detection, online proctoring, cross-device authentication and privacy-conscious identity verification, where reducing raw visual data exposure must be weighed against operational discriminability.

Our contributions are as follows. First, we present a dispersion-aware adaptive-margin method that adjusts instance-level margins using feature spread to improve intra-class compactness and cross-camera discrimination. Second, we propose a geometry-conditioned attention mechanism that incorporates camera-layout priors into graph self-attention to achieve spatially consistent alignment across views. Third, we design privacy-calibrated embedding transformations that support efficient indexing and provide formal differential privacy through encoder clipping and calibrated noise. Finally, we demonstrate across standard Re-ID benchmarks that *CityGuard* achieves higher accuracy, stronger robustness to occlusion and domain shift, and stable utility under privacy constraints, indicating suitability for privacy-sensitive deployments.

2 Related Work

2.1 Architectural Foundations and Geometry-Aware Encoders

Person re-identification (ReID) architectures have evolved from early convolutional and generative–discriminative hybrids [20] to transformer-based and multi-scale designs that better capture global context and fine-grained spatial cues [5, 21, 6, 7]. Recent efforts also emphasize efficiency and deployment feasibility, introducing lightweight transformer variants for edge scenarios [22] and compact 3D-aware representations to mitigate viewpoint sensitivity [4, 23]. Additionally, spatially structured attention mechanisms, such as group-aware and multi-view encoders [24, 25], motivate our use of geometry-conditioned graph attention to enhance spatial reasoning across camera views.

2.2 Loss Functions and Distribution-Aware Optimization

The progression of ReID loss functions has shifted from pairwise and triplet-based objectives to margin-driven and contrastive formulations that better structure the embedding space. Foundational works [26, 27] introduced metric-based losses, while recent studies propose adaptive margins and teacher-guided contrastive learning to handle intra-class variability [28, 29]. Dual-graph and group-aware contrastive methods [30] further exploit inter-sample structure, and

dispersion-aware optimization [10] suggests tailoring margins to per-identity variance. *CityGuard* builds on these insights by integrating dispersion-sensitive margins with transport-regularized matching, aligning the loss landscape with both feature spread and geometry-derived camera topology.

2.3 Cross-Modal and Occlusion-Robust Approaches

Robust ReID under modality shifts and occlusion has driven the development of modality-aware encoders, image-text fusion, and clothing-invariant transfer learning [31, 32, 33]. Cross-modal alignment techniques address RGB-D and thermal-visible discrepancies [34, 35], while occlusion-resilient models leverage multi-scale attention, token-level coupling, and synthetic occlusion augmentation to recover partial features [18, 13]. However, these methods often overlook camera topology as a structural prior. In contrast, *CityGuard* explicitly incorporates topological cues to regularize attention and enhance robustness under challenging conditions.

2.4 Adversarial Robustness, Privacy, and Camera Alignment

Beyond accuracy, real-world ReID systems must address adversarial robustness, privacy, and cross-camera consistency. Adversarial alignment [11] and reliability-aware learning [36] mitigate domain shifts from heterogeneous camera setups. Privacy-preserving strategies, including source-free adaptation and differential privacy mechanisms [17, 37], aim to protect identity data. Additionally, defenses against physical and generative attacks [38, 39] highlight the need for resilient representations. *CityGuard* unifies these concerns by embedding privacy-aware features, geometry-guided alignment, and adversarial hardening into a cohesive framework.

2.5 Unsupervised, Self-Supervised, and Source-Free Learning

Efforts to reduce annotation dependency have led to advances in unsupervised and self-supervised ReID. Two-stream pretraining, teacher-student models, and dual-graph contrastive learning [40, 30, 29] provide strong initialization and clustering stability. Source-free adaptation and intra-class variance modeling [10, 41] refine pseudo-labels without source data, often via contrastive learning and online clustering. Despite progress, few methods leverage geometry-induced camera topology to guide clustering or prototype propagation. *CityGuard* addresses this gap by introducing geometry-conditioned graph constraints and dispersion-aware margins, offering a promising direction for source-free and self-supervised ReID.

2.6 Privacy threat models in Re-ID

Re-ID systems face several distinct privacy threats. Membership-inference and similarity-distribution attacks exploit embedding-space statistics to detect whether an image was used for training [42, 43]. Reconstruction and feature-inversion attacks recover visual or attribute information from embeddings [44]. Dataset-enrichment and linkage attacks combine leaked features with auxiliary data to re-identify individuals [45, 46]. Adaptive-query and composition attacks leverage repeated probing of retrieval services, motivating formal privacy accounting and differentially private mechanisms [47]. *CityGuard* assumes an honest-but-curious retrieval adversary and applies layered defenses: encoder clipping for bounded sensitivity, Gaussian noise for per-query differential privacy, online composition accounting, and representation-level hardening with topology-aware aggregation to improve robustness against membership, similarity, and inversion attacks [42, 44, 47].

3 Methodology

We present *CityGuard* as an integrated framework that combines geometry-induced topology-aware geometry encoding, adaptive-margin metric learning, transport-regularized retrieval, temporal graph modeling, and differentially private embedding release. The following subsections describe the problem setup, the geometry-conditioned backbone and attention, the temporal graph network, the dispersion-aware ACT loss with an explicit positive/negative mining strategy, the transport-regularized retrieval term, and the privacy-preserving indexing mechanism. We formalize the adversarial assumptions and differential privacy guarantees in Section A.7.

3.1 Problem setup and retrieval objective

We formulate cross-camera identity association as a retrieval and ranking problem: given a query image \mathcal{I}^q , an encoder Φ computes a d -dimensional embedding $\mathcal{F}^q = \Phi(\mathcal{I}^q)$ and the system returns the top- K gallery items with smallest

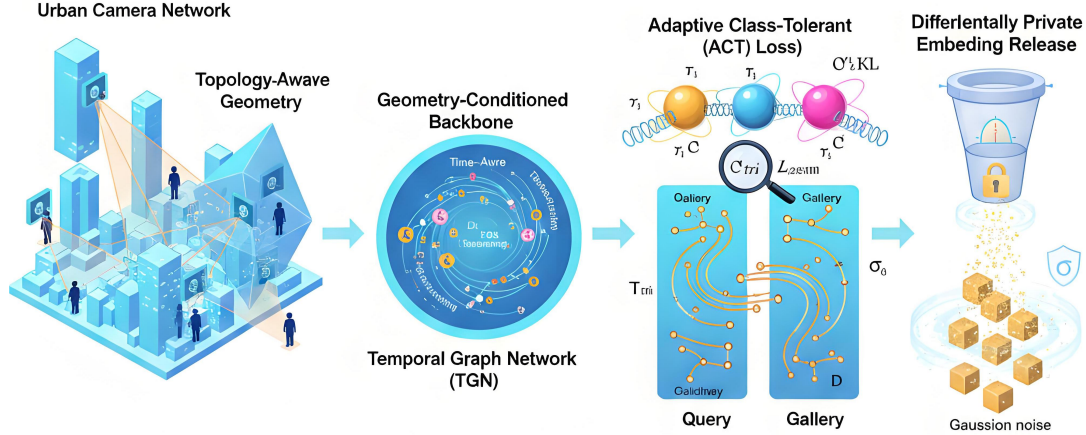


Figure 1: Overview of the **CityGuard** framework for bias-resilient, privacy-preserving identity search. The process begins with **Topology-Aware Geometry Encoding**, where camera coordinates and rotations are mapped to a spatial adjacency graph. The **Geometry-Conditioned Backbone** then fuses multi-scale features and refines them through a **Temporal Graph Network (TGN)** to capture cross-camera motion cues. Centrally, the **Dispersion-Aware Metric Calibration** utilizes an **Adaptive Class-Tolerant (ACT) Loss** to dynamically adjust margins γ_i based on per-identity distribution divergence. Global consistency is enforced via a **Transport-Regularized Retrieval** objective using Sinkhorn iterations. Finally, the **Differentially Private Embedding Release** applies a Gaussian mechanism calibrated by L_2 -sensitivity to produce privatized descriptors \tilde{f} for secure, large-scale indexing.

dissimilarity. Concretely,

$$\hat{S}_K(\mathcal{I}^q) = \text{TopK}_k \delta(\mathcal{F}^q, \mathcal{F}_k^g). \quad (1)$$

where $\hat{S}_K(\mathcal{I}^q)$ denotes the index set of the top- K retrieved gallery items for query \mathcal{I}^q , $\mathcal{F}^q = \Phi(\mathcal{I}^q)$ denotes the d -dimensional embedding returned by the image encoder $\Phi: \mathbb{R}^{H \times W \times 3} \rightarrow \mathbb{R}^d$, $\{\mathcal{F}_k^g\}$ denotes the gallery embeddings, and $\delta(\cdot, \cdot)$ denotes a nonnegative dissimilarity function (in our implementation we use cosine dissimilarity $\delta(u, v) = 1 - \cos(u, v)$).

3.2 Geometry prior for camera layout

To capture coarse camera relationships without requiring survey-grade calibration, we form a geometry-aware Gaussian affinity matrix from available spatial metadata and optionally from relative rotations. The adjacency between camera i and camera j is defined by

$$A_{ij} = \exp\left(-\frac{\|R_{ij}p_i - p_j\|_2^2}{2\sigma^2}\right), \quad (2)$$

where $A \in \mathbb{R}^{N \times N}$ is the adjacency matrix for N cameras, $p_i \in \mathbb{R}^3$ denotes the three-dimensional position of camera i , $R_{ij} \in \text{SO}(3)$ denotes an optional rotation matrix that aligns camera i 's frame to camera j 's frame, $\|\cdot\|_2$ denotes the Euclidean norm, and $\sigma > 0$ is a bandwidth parameter controlling the locality of the geometric prior. When a rotation R_{ij} is not available we set $R_{ij} = I$, the identity matrix. The spatial metadata used to construct p_i and R_{ij} may come from coarse sources such as commodity GPS tags, noisy visual odometry or SLAM estimates, or facility blueprints recorded during installation. These sources typically provide metric-level accuracy rather than precise calibration, which motivates the use of a smooth exponential kernel that is inherently tolerant to moderate coordinate noise. For a perturbation Δp on camera coordinates the affinity evaluated at the perturbed position satisfies

$$A_{ij}(p_i + \Delta p) = \exp\left(-\frac{\|R_{ij}(p_i + \Delta p) - p_j\|_2^2}{2\sigma^2}\right), \quad (3)$$

where the notation $A_{ij}(p_i + \Delta p)$ indicates the dependency of A_{ij} on the perturbed coordinate. Consequently the absolute change in affinity is bounded by

$$|A_{ij}(p_i + \Delta p) - A_{ij}(p_i)| \leq 1 - \exp\left(-\frac{\|\Delta p\|_2^2}{2\sigma^2}\right), \quad (4)$$

where the right-hand side follows from basic algebraic manipulation of the kernel and the monotonicity of the exponential function. For perturbations satisfying $\|\Delta p\|_2 \ll \sigma$ the bound in (4) is approximately $\|\Delta p\|_2^2 / (2\sigma^2)$, which demonstrates second-order insensitivity to small coordinate noise. We validate these robustness properties empirically in the ablation studies. When the coordinate noise magnitude is below 0.5 meters and the bandwidth is chosen as $\sigma \geq 5$ meters, retrieval performance remains stable in our experiments. Thus coarse spatial metadata suffice to induce a useful camera graph, and expensive external calibration is not required for effective geometry-conditioned attention.

3.3 Integrated backbone and multi-scale fusion

Our encoder is staged so that successive modules extract hierarchical representations while preserving local detail; the cascade is expressed as

$$\mathcal{F} = \Gamma_S \circ \Gamma_{S-1} \circ \dots \circ \Gamma_1(\mathcal{I}). \quad (5)$$

where $\mathcal{I} \in \mathbb{R}^{H \times W \times 3}$ denotes the input image, $\Gamma_s(\cdot)$ denotes the transformation at stage s (for example convolutional blocks or transformer layers), and $\mathcal{F} \in \mathbb{R}^{h \times w \times d}$ denotes the resulting feature tensor.

To combine multi-scale cues we apply a simple upsample-and-add fusion:

$$\mathcal{F}_s^{\text{fused}} = \mathcal{C}_{1 \times 1}(\mathcal{U}_{\times 2}(\mathcal{F}_s)) \oplus \mathcal{F}_{s-1}^\downarrow, \quad (6)$$

where $\mathcal{U}_{\times 2}$ denotes bilinear upsampling by a factor of two, $\mathcal{C}_{1 \times 1}$ denotes a 1×1 convolution used to align channel dimensions, $\mathcal{F}_{s-1}^\downarrow$ denotes the adjacent coarser-scale feature after optional downsampling, and \oplus denotes element-wise addition.

3.4 Geometry-conditioned attention

We bias attention logits by geometry-weighted context so that spatial proximity increases cross-node interactions:

$$\mathcal{A} = \text{softmax}\left(\frac{(XW_q)(CW_k)^\top}{\sqrt{d}} + B_{\text{geom}}\right). \quad (7)$$

where $X \in \mathbb{R}^{N \times d}$ denotes the matrix of node features with one row per camera node, $W_q, W_k \in \mathbb{R}^{d \times d}$ denote learnable linear projections for queries and keys respectively, $C \in \mathbb{R}^{N \times d}$ denotes the geometry-weighted context matrix usually computed as $C_i = \sum_j s(A_{ij})\Theta X_j$ for a normalization $s(\cdot)$ and linear map Θ , $B_{\text{geom}} \in \mathbb{R}^{N \times N}$ denotes a geometry-derived bias (implemented as a deterministic function of $\log A$ or as a learnable residual), and the row-wise softmax produces attention weights that sum to one per query node. After computing attention we refine node features with a residual update:

$$\hat{X} = \mathcal{A}(XW_v) \oplus X, \quad (8)$$

where $W_v \in \mathbb{R}^{d \times d}$ denotes the value projection and \oplus denotes element-wise residual addition that stabilizes optimization while preserving the original representations.

3.5 Temporal modeling via a Temporal Graph Network (TGN)

Temporal correlations and cross-camera motion cues are incorporated by a message-passing TGN that aggregates neighborhood information across time:

$$\mathbf{m}_{ij} = \phi_m(\mathcal{F}_{t-\tau}^{(i)}, \mathcal{F}_{t-\tau}^{(j)}, e_{ij}), \quad (9)$$

$$\mathbf{a}_i = \phi_a(\{\mathbf{m}_{ij}\}_{j \in \mathcal{N}(i)}, \mathcal{F}_{t-\tau}^{(i)}), \quad (10)$$

$$\mathcal{F}_t^{\text{temp}} = \Psi_{\text{TGN}}(\{\mathcal{F}_{t-\tau}^{(i)}\}_{i=1}^N; \tau), \quad (11)$$

where \mathbf{m}_{ij} denotes the message from node i to node j at temporal lag τ , $\phi_m(\cdot)$ denotes a small multi-layer perceptron that computes pairwise messages conditioned on an edge descriptor e_{ij} , $\mathcal{N}(i)$ denotes the neighborhood of node i in the camera graph, $\phi_a(\cdot)$ denotes the aggregation function that combines incoming messages with node priors to produce updated context \mathbf{a}_i , and $\Psi_{\text{TGN}}(\cdot)$ denotes the overall TGN operator that returns time-conditioned features $\mathcal{F}_t^{\text{temp}}$.

3.6 Dispersion-aware metric calibration and the ACT loss

To adapt margins to per-identity dispersion we measure divergence between an identity’s empirical distribution and a global reference and set an instance margin accordingly:

$$\gamma_i = \gamma_0(1 + \alpha \tanh(\beta \mathcal{D}_{\text{KL}}(P_i \parallel Q))). \quad (12)$$

where γ_i denotes the adaptive margin for identity i , $\gamma_0 > 0$ denotes the base margin, $\alpha > 0$ and $\beta > 0$ are hyperparameters controlling scale and sensitivity of the adaptation, $\mathcal{D}_{\text{KL}}(P_i \parallel Q)$ denotes the Kullback–Leibler divergence between the empirical feature distribution P_i for identity i and the global feature distribution Q aggregated across identities. Using the per-identity margin we define the Adaptive Class-Tolerant (ACT) objective which combines an additive-angular-margin identification term and a margin-adaptive triplet term with an explicit hardest-mining strategy. The overall ACT loss for a mini-batch is

$$\mathcal{L}_{\text{ACT}} = \mathcal{L}_{\text{ID}}^{\text{ACT}} + \lambda_{\text{tri}} \mathcal{L}_{\text{tri}}^{\text{ACT}}, \quad (13)$$

where $\lambda_{\text{tri}} \geq 0$ is a weighting scalar that balances the triplet component.

The adaptive identification term is an additive-angular-margin softmax with class-conditioned margins:

$$\mathcal{L}_{\text{ID}}^{\text{ACT}} = -\frac{1}{N} \sum_{i=1}^N \log \frac{\exp(s(\cos \theta_{i,y_i} - \gamma_{y_i}))}{\exp(s(\cos \theta_{i,y_i} - \gamma_{y_i})) + \sum_{j \neq y_i} \exp(s \cos \theta_{i,j})}. \quad (14)$$

where N denotes the batch size, $\cos \theta_{i,j} = \langle f_i, w_j \rangle / (\|f_i\| \|w_j\|)$ denotes the cosine similarity between the normalized feature f_i of sample i and the class prototype w_j , y_i denotes the ground-truth class of sample i , $s > 0$ is a scaling factor applied to logits, and γ_{y_i} denotes the adaptive margin for class y_i as in Eq. (12).

The adaptive triplet term performs hard positive and semi-hard negative mining within the mini-batch and uses the per-class margin in the hinge:

$$\mathcal{L}_{\text{tri}}^{\text{ACT}} = \frac{1}{N} \sum_{i=1}^N [\delta(f_i, f_{p^*(i)}) - \delta(f_i, f_{n^*(i)}) + \gamma_{y_i}]_+, \quad (15)$$

where $[\cdot]_+ = \max(0, \cdot)$ denotes the hinge operator, $\delta(\cdot, \cdot)$ denotes the pairwise dissimilarity used in retrieval (we use cosine dissimilarity $1 - \cos(\cdot, \cdot)$), and γ_{y_i} denotes the per-class adaptive margin.

For each anchor i the hardest positive in the batch is selected as

$$p^*(i) = \arg \max_{p \in \mathcal{P}(i)} \delta(f_i, f_p), \quad (16)$$

where $\mathcal{P}(i) = \{p \mid y_p = y_i, p \neq i\}$ denotes the set of same-identity examples in the current batch and $p^*(i)$ denotes the one with maximal dissimilarity to the anchor i .

The semi-hard negative is selected as

$$n^*(i) = \arg \min_{n \in \mathcal{N}(i)} \left\{ \delta(f_i, f_n) : \delta(f_i, f_n) > \delta(f_i, f_{p^*(i)}) \right\}. \quad (17)$$

where $\mathcal{N}(i) = \{n \mid y_n \neq y_i\}$ denotes the set of different-identity examples in the batch and $n^*(i)$ denotes the nearest negative whose dissimilarity exceeds the hardest-positive distance (if no such semi-hard negative exists we fall back to the batch-global minimum negative). The mining rules in Eqs. (16)–(17) are implemented efficiently using matrix operations on the batch-wise distance matrix to avoid loops.

3.7 Transport-regularized retrieval objective

To encourage database-aware global matching we adopt an entropic optimal transport objective with a marginal divergence penalty:

$$\mathcal{L}_{\text{OT}} = \min_{\mathbf{T} \in \Pi(\mathbf{p}, \mathbf{q})} \langle \mathbf{T}, \mathbf{D} \rangle + \epsilon \sum_{i,j} T_{ij} (\log T_{ij} - 1) + \lambda \mathcal{D}_{\text{KL}}(\mathbf{p} \parallel \mathbf{q}). \quad (18)$$

where $\mathbf{D} \in \mathbb{R}^{n \times m}$ denotes the pairwise dissimilarity matrix with entries $D_{ij} = \delta(f_i, f_j)$ computed on the current batch or merged pseudo-batches, $\mathbf{T} \in \mathbb{R}^{n \times m}$ denotes the transport plan constrained to the transportation polytope $\Pi(\mathbf{p}, \mathbf{q})$ with marginals \mathbf{p} and \mathbf{q} , $\epsilon > 0$ controls the entropic regularization which stabilizes and accelerates Sinkhorn iterations, and $\lambda \geq 0$ weights the marginal KL penalty.

3.8 Generalization control (informal data-dependent statement)

We provide a data-dependent control that highlights the dependence of sampling error on per-identity divergence; under standard concentration assumptions we obtain the following informal statement:

$$\mathcal{R}(\gamma_i) \leq \mathcal{R}_n(\gamma_i) + C \sqrt{\frac{\mathcal{D}_{\text{KL}}(P_i \parallel Q)}{n}}, \quad (19)$$

where $\mathcal{R}(\gamma_i)$ denotes the population risk under margin γ_i , $\mathcal{R}_n(\gamma_i)$ denotes the empirical risk computed on n i.i.d. samples, $\mathcal{D}_{\text{KL}}(P_i \parallel Q)$ denotes the Kullback–Leibler divergence between the per-identity distribution P_i and the global reference Q , and $C > 0$ denotes a constant that depends on model capacity and concentration constants; a rigorous proof and the technical assumptions are provided in the Appendix A.1.

3.9 Differentially private embedding release and indexing

To protect stored embeddings we apply the Gaussian mechanism to encoder outputs and calibrate the noise according to (ϵ, δ) -DP:

$$\mathcal{M}(X) = f(X) + \mathcal{N}(0, \sigma^2 S_f^2 I), \quad (20)$$

where $f(X)$ denotes the deterministic encoder mapping applied to input X , S_f denotes the L_2 -sensitivity of f under the chosen threat model, I denotes the identity matrix of appropriate dimension, and the additive noise is isotropic Gaussian with per-coordinate variance $\sigma^2 S_f^2$. The noise multiplier is chosen according to the standard Gaussian mechanism:

$$\sigma \geq \frac{\sqrt{2 \ln(1.25/\delta)} S_f}{\epsilon}, \quad (21)$$

where $\epsilon > 0$ denotes the privacy budget and $\delta \in (0, 1)$ denotes the allowed failure probability for (ϵ, δ) -differential privacy.

Algorithm 1 CityGuard: Topology-Guided Private Embeddings for Multi-Camera Retrieval

Require: Image set \mathcal{I} , camera coordinates $\{p_i\}_{i=1}^N$, optional rotations $\{R_{ij}\}$, per-query privacy budget (ϵ, δ) , index hyperparameters, training hyperparameters.

Ensure: Privatized index and trained encoder Φ for online retrieval and privacy accounting module $\mathcal{A}ct$.

- 1: **Initialize:** encoder Φ , attention weights $\{W_q, W_k, W_v\}$, prototypes $\{w_j\}$, OT params $(\epsilon_{\text{OT}}, \lambda)$, ACT hyperparams $(\gamma_0, \alpha, \beta, s, \lambda_{\text{tri}})$, clipping radius B .
 - 2: Build camera adjacency A via Eq. (2).
 - 3: **for** epoch = 1, . . . , E **do**
 - 4: **for** each mini-batch $\mathcal{B} \subset \mathcal{I}$ **do**
 - 5: Compute multi-scale features $\{\mathcal{F}_s\}$ via Eq. (5).
 - 6: Fuse scales to obtain $\mathcal{F}^{\text{fused}}$ via Eq. (6).
 - 7: Form node-feature matrix X with one row per camera / node.
 - 8: Compute geometry-weighted context C and geometry bias B_{geom} .
 - 9: Compute attention \mathcal{A} via Eq. (7) and refine node features \hat{X} via Eq. (8).
 - 10: Maintain running estimates of per-identity distributions $\{P_i\}$ and global prior Q .
 - 11: Update adaptive margins γ_i via Eq. (12).
 - 12: Compute ACT loss \mathcal{L}_{ACT} (Eqs. (13)–(15)) with hard-positive / semi-hard-negative mining.
 - 13: Build dissimilarity matrix \mathbf{D} and compute OT loss \mathcal{L}_{OT} via Sinkhorn (Eq. (18)).
 - 14: $\mathcal{L}_{\text{total}} \leftarrow \mathcal{L}_{\text{ACT}} + \lambda_{\text{OT}} \mathcal{L}_{\text{OT}} + \lambda_{\text{aux}} \mathcal{L}_{\text{aux}}$.
 - 15: Backpropagate and update Φ , attention weights, and prototypes.
 - 16: **end for**
 - 17: **if** periodic **then**
 - 18: Re-estimate encoder L_2 -sensitivity S_f according to Eq. (71).
 - 19: Compute per-query noise scale σ by Eq. (73) and update privacy accountant $\mathcal{A}ct$.
 - 20: Optionally adjust training (e.g., clipping radius B) to meet sensitivity targets.
 - 21: **end if**
 - 22: **end for**
 - 23: **Stage III: Privatize and build index**
 - 24: For each gallery embedding f , clip $\bar{f} = \text{Clip}_B(f)$ and draw $\tilde{f} = \bar{f} + \mathcal{N}(0, \sigma^2 I)$.
 - 25: Build approximate index (e.g., PQ or HNSW) on $\{\tilde{f}\}$ and set retrieval parameters.
 - 26: Deploy privacy accountant $\mathcal{A}ct$ to track cumulative $(\epsilon_{\text{total}}, \delta_{\text{total}})$ and enforce query budget limits.
 - 27: **return** privatized index, final encoder Φ , and accountant $\mathcal{A}ct$.
-

3.10 Training schedule and full objective

The full training objective used in experiments combines the ACT loss, the transport-regularized retrieval term, and optional auxiliary losses for self-supervision and reconstruction:

$$\mathcal{L}_{\text{total}} = \mathcal{L}_{\text{ACT}} + \lambda_{\text{OT}}\mathcal{L}_{\text{OT}} + \lambda_{\text{aux}}\mathcal{L}_{\text{aux}}, \quad (22)$$

where λ_{OT} and λ_{aux} are nonnegative scalars balancing the transport term and auxiliary heads respectively, and \mathcal{L}_{ACT} is defined in Eq. (13). Training proceeds in three logical phases: in the representation pretraining phase we optimize the backbone and geometry-conditioned attention on labeled source data with the ACT objective and auxiliary classification heads; in the adaptation and privacy calibration phase we adapt embeddings to the target gallery distribution while estimating S_f and tuning (ϵ, δ) ; finally, in the deployment phase we privatize embeddings using Eq. (20) and construct efficient similarity indexes (e.g., HNSW or PQ) for online retrieval.

3.11 Interpretability and diagnostics

For introspection we compute gradient-weighted attention saliency maps:

$$\mathcal{S} = \text{ReLU}\left(\sum_k \frac{1}{Z_k} \sum_{i,j} \frac{\partial y}{\partial A_{ij}^k} A^k\right), \quad (23)$$

where A^k denotes the k -th attention-head matrix, Z_k denotes a head-specific normalization constant, $\partial y / \partial A_{ij}^k$ denotes the gradient of the model score y with respect to attention entry A_{ij}^k , and ReLU denotes the rectified linear unit which suppresses negative contributions for clearer visualization. To quantify embedding compactness we report

$$\mathcal{Q} = \frac{1}{K} \sum_{i=1}^K \left[\frac{1}{|C_i|} \sum_{x \in C_i} \|x - \mu_i\|_2 - \min_{j \neq i} \|\mu_i - \mu_j\|_2 \right], \quad (24)$$

where K denotes the number of identity clusters, C_i denotes the sample set for cluster i , μ_i denotes the centroid of cluster i , and $\|\cdot\|_2$ denotes the Euclidean norm; lower values of \mathcal{Q} indicate tighter intra-class grouping relative to inter-class separation.

4 Experiment

4.1 Datasets and evaluation metrics

We evaluate CityGuard on standard person re-identification benchmarks: Market-1501[48], MARS[49], MSMT17 [50], RegDB[51], SYSU-MM01[52], Occluded-REID[53], Partial-REID[54], and Partial-iLIDS[55]. Performance is reported using Rank- k (typically Rank-1), mean Average Precision (mAP) and mean Inverse Negative Penalty (mINP) to capture both retrieval accuracy and ranking robustness. These datasets collectively span diverse capture conditions, camera geometries and cross-spectral scenarios, which allows us to measure retrieval quality under realistic deployment heterogeneity.

4.2 Implementation details

All experiments are implemented in PyTorch and run on four NVIDIA V100 GPUs. We evaluate ResNet-50, DenseNet-161, Swin-T, and HRNet-W48 backbones. Models are trained for 120 epochs with AdamW, a global batch size of 192, and standard Re-ID augmentations (random crop, horizontal flip, color jitter, random erasing). For retrieval profiling, we benchmark common approximate nearest neighbor indexes and GPU-accelerated query kernels; latency and GFLOPS are measured at 128×64 resolution unless stated otherwise. Differential privacy bounds membership-inference risk, consistent with our empirical results (App. J).

As shown in App. I, reducing ϵ yields predictable utility degradation while maintaining practical retrieval accuracy. All tabular results are reported as mean \pm standard deviation over 5 runs with different seeds, and improvements are validated via paired t-tests ($p < 0.05$). CityGuard demonstrates strong zero-shot cross-domain generalization (Sec. H), delivers reduced database-side latency and index size with PG-Strom (Sec. L), achieves state-of-the-art visible-infrared performance (Sec. G), reduces demographic fairness disparities (Sec. K), forms compact geometry-aware representations (Sec. D), and maintains an efficient accuracy-cost trade-off (Sec. E).

Table 1: Progressive component ablation on Market-1501 and MARS (R1 and mAP only). † denotes removal of geometric prior. * denotes robustness to approximate geometry (coarse GPS or identity rotation).

Configuration	Market R1	Market mAP	MARS R1	MARS mAP
Baseline (Swin-T)	87.6	79.5	84.2	78.3
+ ACT Loss	91.2	82.4	87.1	81.4
+ Geo-Attention	89.8	81.1	86.5	80.1
+ OT Loss	94.5	93.2	94.1	89.3
Full CityGuard (perfect calibration)	97.5	96.5	95.7	91.6
Full CityGuard (w/ coarse GPS noise $\sigma=5m$)*	97.1	96.2	95.4	91.1
Full CityGuard (w/o rotation $R_{ij} = I$)*	96.8	95.9	95.1	90.8
Full † (w/o geometry)	95.2	94.1	93.1	88.4

4.3 Ablation and loss study

Table 1 summarizes an ablation on Market-1501 and a loss-function comparison on MARS. Introducing the adaptive metric consistently improves retrieval performance over the baseline, and incorporating geometry-based alignment further provides complementary benefits. The integrated CityGuard framework, which brings together geometry-conditioned attention, the ACT objective, and adaptive margin control, achieves the most robust results on Market-1501. On MARS the ACT formulation surpasses conventional metric-learning losses, indicating that variance-aware margin adjustment works effectively when combined with spatial priors.

Video Sequence Benchmarking Systematic evaluation of the CityGuard architecture is performed on large-scale video re-identification corpora, benchmarking against leading state-of-the-art algorithms. Empirical findings are catalogued in Table 2. The proposed approach exhibits substantial performance gains over competing methodologies regarding temporal feature aggregation and viewpoint-invariant matching. Such outcomes substantiate the validity of integrating spatial topological priors with differentially private representations within distributed surveillance infrastructures.

Table 2: Comparative performance evaluation on MARS and Market-1501 datasets.

Method	MARS-mAP (%)	MARS-R1 (%)	Market-R1 (%)	Market-mAP (%)
AuxIMD[56]	78.5	87.0	80.9	72.4
STE-NVAN[57]	82.3	88.5	90.0	82.8
HMN[58]	85.1	90.1	93.1	83.3
STA[59]	85.1	89.8	86.3	80.8
COSAM[60]	82.9	90.2	86.9	87.4
GLTR[61]	85.8	90.0	87.0	78.5
VRSTC[62]	85.9	88.8	88.5	82.3
VSFE[63]	86.0	90.2	95.1	87.9
CSSA[41]	84.8	91.0	95.7	88.0
STFE[64]	86.1	90.3	95.5	91.5
DOAN[65]	84.5	90.5	95.7	89.9
PartFormer[66]	87.0	90.8	90.7	96.1
SVDNet[67]	86.2	91.0	82.3	62.1
TransReID[5]	87.2	90.8	95.2	89.5
OAT[68]	87.6	91.7	95.7	89.9
ChatReID[69]	87.0	90.8	97.2	96.4
KWF[70]	86.1	90.3	96.1	90.8
FAA-Net[71]	84.5	90.5	89.6	96.1
DTC-CINet[72]	87.2	90.8	95.2	87.8
TCViT[73]	87.6	91.7	91.7	83.1
CityGuard	91.6	95.7	97.5	96.5

4.4 Comparative Performance Analysis on Occluded and Partial Re-ID Benchmarks

We provide a comparative evaluation of CityGuard and existing methods on occluded and partial person re-identification benchmarks. For detailed results and analysis, please refer to Appendix F.

4.5 Analysis, Robustness, and Failure Modes

Our comprehensive experimental analysis demonstrates that the synergistic integration of geometry-conditioned feature learning and dispersion-aware metric calibration within the CityGuard framework effectively mitigates cross-view distribution shifts and enhances feature separability, particularly under challenging conditions characterized by high intra-class variance. The proposed Adaptive Class-Tolerant (ACT) loss further refines the embedding geometry, promoting compact intra-class clusters and improved inter-class separation, as quantitatively evidenced by our results.

Table 3: Adversarial robustness evaluation of *CityGuard* and baseline methods on Market-1501 and MSMT17 under FGSM ($\epsilon = 4/255$) and PGD-20 ($\epsilon = 4/255$, step size=1/255) attacks.

Method	Market-1501			MSMT17		
	Clean Rank-1/mAP	FGSM Rank-1/mAP	PGD-20 Rank-1/mAP	Clean Rank-1/mAP	FGSM Rank-1/mAP	PGD-20 Rank-1/mAP
TransReID[5]	95.2/89.5	12.3/5.1	3.7/1.2	83.5/64.4	15.8/6.9	5.4/2.1
OAT[68]	95.7/89.9	18.4/7.3	6.2/2.4	91.2/82.3	19.1/8.5	7.1/2.9
FED[74]	95.0/86.3	22.7/9.8	8.9/3.7	86.3/79.3	24.5/10.2	9.3/3.8
CityGuard (Ours)	97.5/96.5	68.7/52.4	45.2/31.8	94.9/90.1	71.3/55.1	48.9/35.3

To evaluate adversarial robustness, which is essential for secure ReID applications, we conducted white-box attacks using FGSM ($\epsilon = 4/255$) and PGD-20 (step size 1/255) on 1,000 test images from the Market-1501 and MSMT17 datasets. As shown in Table 3, *CityGuard* consistently outperforms strong baselines under both attacks, maintaining higher Rank-1 and mAP scores. This resilience stems from its geometry-aware graph attention and adaptive margin design, which disrupt gradient-based perturbations more effectively than conventional models. Beyond adversarial robustness, *CityGuard* demonstrates strong generalization under occlusion and domain shifts, reinforcing its suitability for real-world deployment. Sensitivity analysis indicates that while optimizer and batch size affect backbone performance, the adaptive margin mechanism remains stable. Failure cases primarily arise under extreme occlusion, severe lighting variation, or near-identical clothing, which degrade feature distinctiveness.

5 Conclusion

We have presented CityGuard, a geometry-induced topology-aware framework for privacy-conscious person re-identification across distributed camera networks. By combining geometry-conditioned attention, dispersion-adaptive margins, and differentially private embedding transforms, the proposed system attains strong retrieval performance while addressing core challenges in privacy, robustness and scalability. Empirical results show that CityGuard consistently improves accuracy relative to competitive baselines and preserves discrimination under occlusion and domain shift. The framework also maintains stable behavior under adversarial perturbations and supports efficient, latency-aware retrieval through compact approximate indexing. Its modular design enables federated adaptation and region-aware policy enforcement, which facilitates practical deployment in privacy-sensitive environments such as smart-city infrastructures and authentication systems. Overall, CityGuard connects advances in representation learning with operational and ethical requirements, offering a practical foundation for secure and responsible identity search at scale. Future work will explore tighter privacy-utility bounds, adaptive index maintenance under streaming data, and richer geometry-informed temporal models for continual deployment.

References

- [1] Shilin Zhang and Hangbin Yu. Person re-identification by multi-camera networks for internet of things in smart cities. *IEEE Access*, 6:76111–76117, 2018.
- [2] Mang Ye, Jianbing Shen, Gaojie Lin, Tao Xiang, Ling Shao, and Steven CH Hoi. Deep learning for person re-identification: A survey and outlook. *IEEE transactions on pattern analysis and machine intelligence*, 44(6): 2872–2893, 2021.
- [3] Liang Zheng, Yi Yang, and Alexander G Hauptmann. Person re-identification: Past, present and future. *arXiv preprint arXiv:1610.02984*, 2016.
- [4] Zhedong Zheng, Xiaohan Wang, Nenggan Zheng, and Yi Yang. Parameter-efficient person re-identification in the 3d space. *IEEE Transactions on Neural Networks and Learning Systems*, 35(6):7534–7547, 2022.

-
- [5] Shuting He, Hao Luo, Pichao Wang, Fan Wang, Hao Li, and Wei Jiang. Transreid: Transformer-based object re-identification. In *Proceedings of the IEEE/CVF international conference on computer vision*, pages 15013–15022, 2021.
 - [6] Prodip Kumar Sarker, Qingjie Zhao, and Md Kamal Uddin. Transformer-based person re-identification: A comprehensive review. *IEEE Transactions on Intelligent Vehicles*, 9(7):5222–5239, 2024.
 - [7] Bin Hu, Xinggang Wang, and Wenyu Liu. Personvit: large-scale self-supervised vision transformer for person re-identification. *Machine Vision and Applications*, 36(2):32, 2025.
 - [8] Jiayun Wang, Sanping Zhou, Jinjun Wang, and Qiqi Hou. Deep ranking model by large adaptive margin learning for person re-identification. *Pattern Recognition*, 74:241–252, 2018.
 - [9] Qianqian Zhao, Hanxiao Wu, and Jianqing Zhu. Margin-based modal adaptive learning for visible-infrared person re-identification. *Sensors*, 23(3):1426, 2023.
 - [10] Lingzhi Liu, Haiyang Zhang, Chengwei Tang, and Tiantian Zhang. Adaptive intra-class variation contrastive learning for unsupervised person re-identification. *arXiv preprint arXiv:2404.04665*, 2024.
 - [11] Lei Qi, Lei Wang, Jing Huo, Yinghuan Shi, Xin Geng, and Yang Gao. Adversarial camera alignment network for unsupervised cross-camera person re-identification. *IEEE Transactions on Circuits and Systems for Video Technology*, 32(5):2921–2936, 2021.
 - [12] Yuxuan Liu, Hongwei Ge, Guozhi Tang, and Yong Luo. Occluded person re-identification via a universal framework with difference consistency guidance learning. *IEEE Internet of Things Journal*, 2024.
 - [13] Li Wang, Shuli Cheng, Anyu Du, Liejun Wang, and Lun Zhang. Occlusion simulation and token-constrained feature coupling network for occluded person re-identification. *IEEE Internet of Things Journal*, 2025.
 - [14] Dengwen Wang, Guanyu Xing, and Yanli Liu. Texture-aware transformer with pose-patch mapping for occluded person re-identification. *Pattern Recognition*, page 112341, 2025.
 - [15] Shoudong Han, Ziwen Zhang, Xinpeng Yuan, and Delie Ming. Enhance heads in vision transformer for occluded person re-identification. *IEEE Sensors Journal*, 2025.
 - [16] Kajal Kansal, Yongkang Wong, and Mohan Kankanhalli. Privacy-enhancing person re-identification framework—a dual-stage approach. In *Proceedings of the IEEE/CVF Winter Conference on Applications of Computer Vision*, pages 8543–8552, 2024.
 - [17] Xiaofeng Qu, Li Liu, Huaxiang Zhang, Lei Zhu, Liqiang Nie, Xiaojun Chang, and Fengling Li. Secureda: Privacy-preserving source-free domain adaptation for person re-identification. *IEEE Transactions on Multimedia*, 2025.
 - [18] Ming Ma, Jianming Wang, and Bohan Zhao. A multi-scale graph attention-based transformer for occluded person re-identification. *Applied Sciences*, 14(18):8279, 2024.
 - [19] Yue Su, Hao Li, and Maoguo Gong. Generative adversarial patches for physical attacks on cross-modal pedestrian re-identification. *arXiv preprint arXiv:2410.20097*, 2024.
 - [20] Zhedong Zheng, Xiaodong Yang, Zhiding Yu, Liang Zheng, Yi Yang, and Jan Kautz. Joint discriminative and generative learning for person re-identification. In *proceedings of the IEEE/CVF conference on computer vision and pattern recognition*, pages 2138–2147, 2019.
 - [21] Zifei Qin, Peishun Liu, Yibei Liu, Haiping Duan, Feifei Li, and Han Wang. Pedestrian re-identification based on swin transformer. In *2022 3rd International Conference on Big Data, Artificial Intelligence and Internet of Things Engineering (ICBAIE)*, pages 123–129. IEEE, 2022.
 - [22] Meng Sun, Ju Ren, and Yaoxue Zhang. Edgevpr: Transformer-based real-time video person re-identification at the edge. In *2024 IEEE 44th International Conference on Distributed Computing Systems (ICDCS)*, pages 13–24. IEEE, 2024.
 - [23] Ziyue Feng, Liang Yang, Pengsheng Guo, and Bing Li. Cvrecon: Rethinking 3d geometric feature learning for neural reconstruction. In *Proceedings of the IEEE/CVF International Conference on Computer Vision*, pages 17750–17760, 2023.

- [24] Lixiang Xu, Qingzhe Cui, Richang Hong, Wei Xu, Enhong Chen, Xin Yuan, Chenglong Li, and Yuanyan Tang. Group multi-view transformer for 3d shape analysis with spatial encoding. *IEEE Transactions on Multimedia*, 26:9450–9463, 2024.
- [25] Hongyu Sun, Yongcai Wang, Peng Wang, Haoran Deng, Xudong Cai, and Deying Li. Vsformer: Mining correlations in flexible view set for multi-view 3d shape understanding. *IEEE Transactions on Visualization and Computer Graphics*, 31(4):2127–2141, 2024.
- [26] Alexander Hermans, Lucas Beyer, and Bastian Leibe. In defense of the triplet loss for person re-identification. *arXiv preprint arXiv:1703.07737*, 2017.
- [27] Yifan Sun, Changmao Cheng, Yuhan Zhang, Chi Zhang, Liang Zheng, Zhongdao Wang, and Yichen Wei. Circle loss: A unified perspective of pair similarity optimization. In *Proceedings of the IEEE/CVF conference on computer vision and pattern recognition*, pages 6398–6407, 2020.
- [28] Yifan Wang, Pingping Liu, Yijun Lang, Qiuzhan Zhou, and Xue Shan. Learnable dynamic margin in deep metric learning. *Pattern Recognition*, 132:108961, 2022.
- [29] Xiao Teng, Chuan Li, Xueqiong Li, Xinwang Liu, and Long Lan. Tig-cl: teacher-guided individual and group aware contrastive learning for unsupervised person re-identification in internet of things. *IEEE Internet of Things Journal*, 2024.
- [30] Lin Zhang, Ran Song, Yifan Wang, Qian Zhang, and Wei Zhang. Dual-graph contrastive learning for unsupervised person reidentification. *IEEE Transactions on Cognitive and Developmental Systems*, 16(4):1352–1363, 2024.
- [31] Baoguang Qi, Yi Chen, Qiang Liu, Xiaohai He, Linbo Qing, Ray E Sheriff, and Honggang Chen. An image–text dual-channel union network for person re-identification. *IEEE Transactions on Instrumentation and Measurement*, 72:1–16, 2023.
- [32] Qizao Wang, Xuelin Qian, Bin Li, Yanwei Fu, and Xiangyang Xue. Image-text-image knowledge transfer for lifelong person re-identification with hybrid clothing states. *IEEE Transactions on Image Processing*, 2025.
- [33] Changshuo Wang, Shuting He, Meiqing Wu, Siew-Kei Lam, Prayag Tiwari, and Xingyu Gao. Looking clearer with text: A hierarchical context blending network for occluded person re-identification. *IEEE Transactions on Information Forensics and Security*, 2025.
- [34] Hao Liu, Jingjing Wu, Feng Li, Jianguo Jiang, and Richang Hong. Syrer: Synergistic relational reasoning for rgb-d cross-modal re-identification. *IEEE Transactions on Multimedia*, 26:5600–5614, 2023.
- [35] Weiyang Zhang, Jiong Guo, Qiang Liu, Maoyang Zou, Honggang Chen, and Jing Peng. Rxnet: cross-modality person re-identification based on a dual-branch network: W. zhang et al. *Applied Intelligence*, 55(15):993, 2025.
- [36] Zhengqi Liu, Yutian Lin, Tianyang Liu, and Bo Du. Reliable cross-camera learning in random camera person re-identification. *IEEE Transactions on Circuits and Systems for Video Technology*, 34(6):4556–4567, 2023.
- [37] Shafiq Ahmad, Gianluca Scarpellini, Pietro Morerio, and Alessio Del Bue. Event-driven re-id: A new benchmark and method towards privacy-preserving person re-identification. In *Proceedings of the IEEE/CVF winter conference on applications of computer vision*, pages 459–468, 2022.
- [38] Wenli Sun, Xinyang Jiang, Dongsheng Li, and Cairong Zhao. Diffphysba: Diffusion-based physical backdoor attack against person re-identification in real-world. *arXiv preprint arXiv:2405.19990*, 2024.
- [39] Deyin Liu, Lin Wu, Richang Hong, Zongyuan Ge, Jialie Shen, Farid Boussaid, and Mohammed Bennamoun. Generative metric learning for adversarially robust open-world person re-identification. *ACM Transactions on Multimedia Computing, Communications and Applications*, 19(1):1–19, 2023.
- [40] Xi Yang, Liangchen Liu, Nannan Wang, and Xinbo Gao. A two-stream dynamic pyramid representation model for video-based person re-identification. *IEEE Transactions on Image Processing*, 30:6266–6276, 2021.
- [41] Zhidan Ran, Zhiyao Xiao, Xiaobo Lu, Xuan Wei, and Wei Liu. Context-aided semantic-aware self-alignment for video-based person re-identification. *IEEE Transactions on Circuits and Systems for Video Technology*, 2025.
- [42] Junyao Gao, Xinyang Jiang, Huishuai Zhang, Yifan Yang, Shuguang Dou, Dongsheng Li, Duoqian Miao, Cheng Deng, and Cairong Zhao. Similarity distribution based membership inference attack on person re-identification. In *Proceedings of the AAAI conference on artificial intelligence*, volume 37, pages 14820–14828, 2023.

- [43] Junyao Gao, Xinyang Jiang, Shuguang Dou, Dongsheng Li, Duoqian Miao, and Cairong Zhao. Re-id-leak: Membership inference attacks against person re-identification. *International Journal of Computer Vision*, 132(10):4673–4687, 2024.
- [44] Mang Ye, Wei Shen, Junwu Zhang, Yao Yang, and Bo Du. Securereid: Privacy-preserving anonymization for person re-identification. *IEEE Transactions on Information Forensics and Security*, 19:2840–2853, 2024.
- [45] Lamyamba Laishram, Muhammad Shaheryar, Jong Taek Lee, and Soon Ki Jung. Toward a privacy-preserving face recognition system: A survey of leakages and solutions. *ACM Computing Surveys*, 57(6):1–38, 2025.
- [46] Andrea Artioli, Luca Bedogni, and Mauro Leoncini. Re-identification attack based on few-hints dataset enrichment for ubiquitous applications. In *2022 IEEE 8th World Forum on Internet of Things (WF-IoT)*, pages 1–6. IEEE, 2022.
- [47] Lucas Maris, Yuki Matsuda, and Keiichi Yasumoto. Differential privacy and k-anonymity for pedestrian image data: Impact on cross-camera person re-identification and demographic predictions. *ACM Transactions on Cyber-Physical Systems*, 9(4):1–31, 2025.
- [48] Liang Zheng, Liyue Shen, Lu Tian, Shengjin Wang, Jingdong Wang, and Qi Tian. Scalable person re-identification: A benchmark. In *Proceedings of the IEEE international conference on computer vision*, pages 1116–1124, 2015.
- [49] Liang Zheng, Zhi Bie, Yifan Sun, Jingdong Wang, Chi Su, Shengjin Wang, and Qi Tian. Mars: A video benchmark for large-scale person re-identification. In *European conference on computer vision*, pages 868–884. Springer, 2016.
- [50] Longhui Wei, Shiliang Zhang, Wen Gao, and Qi Tian. Person transfer gan to bridge domain gap for person re-identification. In *Proceedings of the IEEE conference on computer vision and pattern recognition*, pages 79–88, 2018.
- [51] Dat Tien Nguyen, Hyung Gil Hong, Ki Wan Kim, and Kang Ryoung Park. Person recognition system based on a combination of body images from visible light and thermal cameras. *Sensors*, 17(3):605, 2017.
- [52] Ancong Wu, Wei-Shi Zheng, Hong-Xing Yu, Shaogang Gong, and Jianhuang Lai. Rgb-infrared cross-modality person re-identification. In *Proceedings of the IEEE international conference on computer vision*, pages 5380–5389, 2017.
- [53] Jiakuan Zhuo, Zeyu Chen, Jianhuang Lai, and Guangcong Wang. Occluded person re-identification. In *2018 IEEE international conference on multimedia and expo (ICME)*, pages 1–6. IEEE, 2018.
- [54] Wei-Shi Zheng, Xiang Li, Tao Xiang, Shengcai Liao, Jianhuang Lai, and Shaogang Gong. Partial person re-identification. In *Proceedings of the IEEE international conference on computer vision*, pages 4678–4686, 2015.
- [55] Lingxiao He, Jian Liang, Haiqing Li, and Zhenan Sun. Deep spatial feature reconstruction for partial person re-identification: Alignment-free approach. In *Proceedings of the IEEE conference on computer vision and pattern recognition*, pages 7073–7082, 2018.
- [56] Hehan Teng, Tao He, Yuchen Guo, and Guiguang Ding. A high-accuracy unsupervised person re-identification method using auxiliary information mined from datasets. *arXiv preprint arXiv:2205.03124*, 2022.
- [57] Chih-Ting Liu, Chih-Wei Wu, Yu-Chiang Frank Wang, and Shao-Yi Chien. Spatially and temporally efficient non-local attention network for video-based person re-identification. *arXiv preprint arXiv:1908.01683*, 2019.
- [58] Zhikang Wang, Lihuo He, Xiaoguang Tu, Jian Zhao, Xinbo Gao, Shengmei Shen, and Jiashi Feng. Robust video-based person re-identification by hierarchical mining. *IEEE Transactions on Circuits and Systems for Video Technology*, 32(12):8179–8191, 2021.
- [59] Yang Fu, Xiaoyang Wang, Yunchao Wei, and Thomas Huang. Sta: Spatial-temporal attention for large-scale video-based person re-identification. In *Proceedings of the AAAI conference on artificial intelligence*, volume 33, pages 8287–8294, 2019.
- [60] Arulkumar Subramaniam, Athira Nambiar, and Anurag Mittal. Co-segmentation inspired attention networks for video-based person re-identification. In *Proceedings of the IEEE/CVF international conference on computer vision*, pages 562–572, 2019.

- [61] Jianing Li, Jingdong Wang, Qi Tian, Wen Gao, and Shiliang Zhang. Global-local temporal representations for video person re-identification. In *Proceedings of the IEEE/CVF international conference on computer vision*, pages 3958–3967, 2019.
- [62] Ruibing Hou, Bingpeng Ma, Hong Chang, Xinqian Gu, Shiguang Shan, and Xilin Chen. Vrstc: Occlusion-free video person re-identification. In *Proceedings of the IEEE/CVF conference on computer vision and pattern recognition*, pages 7183–7192, 2019.
- [63] Zunwang Ke, Guozhi Sun, Run Guo, Minghua Du, and Yugui Zhang. Person re-identification method based on video spatial feature enhancement. In *2024 IEEE International Conference on Cognitive Computing and Complex Data (ICCD)*, pages 23–30. IEEE, 2024.
- [64] Xi Yang, Xian Wang, Liangchen Liu, Nannan Wang, and Xinbo Gao. Sfte: a comprehensive video-based person re-identification network based on spatio-temporal feature enhancement. *IEEE Transactions on Multimedia*, 26: 7237–7249, 2024.
- [65] Bo Sun, Yulong Zhang, Jianan Wang, and Chunmao Jiang. Dual-branch occlusion-aware semantic part-features extraction network for occluded person re-identification. *Mathematics*, 13(15):2432, 2025.
- [66] Lei Tan, Pingyang Dai, Jie Chen, Liujuan Cao, Yongjian Wu, and Rongrong Ji. Partformer: Awakening latent diverse representation from vision transformer for object re-identification. *arXiv preprint arXiv:2408.16684*, 2024.
- [67] Yifan Sun, Liang Zheng, Weijian Deng, and Shengjin Wang. Svdnet for pedestrian retrieval. In *Proceedings of the IEEE international conference on computer vision*, pages 3800–3808, 2017.
- [68] Yanping Li, Yizhang Liu, Hongyun Zhang, Cairong Zhao, Zhihua Wei, and Duoqian Miao. Occlusion-aware transformer with second-order attention for person re-identification. *IEEE Transactions on Image Processing*, 2024.
- [69] Ke Niu, Haiyang Yu, Mengyang Zhao, Teng Fu, Siyang Yi, Wei Lu, Bin Li, Xuelin Qian, and Xiangyang Xue. Chatreid: Open-ended interactive person retrieval via hierarchical progressive tuning for vision language models. *arXiv preprint arXiv:2502.19958*, 2025.
- [70] Quang-Huy Che, Le-Chuong Nguyen, Gia-Nghia Tran, Dinh-Duy Phan, and Vinh-Tiep Nguyen. A re-ranking method using k-nearest weighted fusion for person re-identification. *arXiv preprint arXiv:2509.04050*, 2025.
- [71] Yangqi Zheng, Liang Zhang, and Jun Liang. Faa-net: enhancing person re-identification through local-global feature association attention. *Soft Computing*, pages 1–15, 2025.
- [72] Jingyi Wen. Dtc-cinet: Dynamic token compensation and cross-layer interaction network for occluded person re-identification. In *2025 IEEE 3rd International Conference on Image Processing and Computer Applications (ICIPCA)*, pages 214–222. IEEE, 2025.
- [73] Pengfei Wu, Le Wang, Sanping Zhou, Gang Hua, and Changyin Sun. Temporal correlation vision transformer for video person re-identification. In *Proceedings of the AAAI Conference on Artificial Intelligence*, volume 38, pages 6083–6091, 2024.
- [74] Zhikang Wang, Feng Zhu, Shixiang Tang, Rui Zhao, Lihuo He, and Jiangning Song. Feature erasing and diffusion network for occluded person re-identification. In *Proceedings of the IEEE/CVF conference on computer vision and pattern recognition*, pages 4754–4763, 2022.
- [75] David A McAllester. Pac-bayesian model averaging. In *Proceedings of the twelfth annual conference on Computational learning theory*, pages 164–170, 1999.
- [76] Pascal Germain, Francis Bach, Alexandre Lacoste, and Simon Lacoste-Julien. Pac-bayesian theory meets bayesian inference. *Advances in Neural Information Processing Systems*, 29, 2016.
- [77] Yifan Sun, Liang Zheng, Yi Yang, Qi Tian, and Shengjin Wang. Beyond part models: Person retrieval with refined part pooling (and a strong convolutional baseline). In *Proceedings of the European conference on computer vision (ECCV)*, pages 480–496, 2018.

- [78] Guan'an Wang, Shuo Yang, Huanyu Liu, Zhicheng Wang, Yang Yang, Shuliang Wang, Gang Yu, Erjin Zhou, and Jian Sun. High-order information matters: Learning relation and topology for occluded person re-identification. In *Proceedings of the IEEE/CVF conference on computer vision and pattern recognition*, pages 6449–6458, 2020.
- [79] Pengfei Wang, Changxing Ding, Zhiyin Shao, Zhibin Hong, Shengli Zhang, and Dacheng Tao. Quality-aware part models for occluded person re-identification. *IEEE Transactions on Multimedia*, 25:3154–3165, 2022.
- [80] Meiyang Huang, Chunping Hou, Qingyuan Yang, and Zhipeng Wang. Reasoning and tuning: Graph attention network for occluded person re-identification. *IEEE Transactions on Image Processing*, 32:1568–1582, 2023.
- [81] Gang Yan, Zijin Wang, Shuze Geng, Yang Yu, and Yingchun Guo. Part-based representation enhancement for occluded person re-identification. *IEEE Transactions on Circuits and Systems for Video Technology*, 33(8):4217–4231, 2023.
- [82] Yulin Li, Jianfeng He, Tianzhu Zhang, Xiang Liu, Yongdong Zhang, and Feng Wu. Diverse part discovery: Occluded person re-identification with part-aware transformer. In *Proceedings of the IEEE/CVF conference on computer vision and pattern recognition*, pages 2898–2907, 2021.
- [83] Tao Wang, Hong Liu, Pinhao Song, Tianyu Guo, and Wei Shi. Pose-guided feature disentangling for occluded person re-identification based on transformer. In *Proceedings of the AAAI conference on artificial intelligence*, volume 36, pages 2540–2549, 2022.
- [84] Boqiang Xu, Lingxiao He, Jian Liang, and Zhenan Sun. Learning feature recovery transformer for occluded person re-identification. *IEEE Transactions on Image Processing*, 31:4651–4662, 2022.
- [85] Lei Tan, Pingyang Dai, Rongrong Ji, and Yongjian Wu. Dynamic prototype mask for occluded person re-identification. In *Proceedings of the 30th ACM international conference on multimedia*, pages 531–540, 2022.
- [86] Cairong Zhao, Zefan Qu, Xinyang Jiang, Yuanpeng Tu, and Xiang Bai. Content-adaptive auto-occlusion network for occluded person re-identification. *IEEE Transactions on Image Processing*, 32:4223–4236, 2023.
- [87] Mengxi Jia, Yifan Sun, Yunpeng Zhai, Xinhua Cheng, Yi Yang, and Ying Li. Semi-attention partition for occluded person re-identification. In *Proceedings of the AAAI conference on artificial intelligence*, volume 37, pages 998–1006, 2023.
- [88] Wenfeng Liu, Xudong Wang, Lei Tan, Yan Zhang, Pingyang Dai, Yongjian We, and Rongrong Ji. Learning occlusion disentanglement with fine-grained localization for occluded person re-identification. In *Proceedings of the 31st ACM International Conference on Multimedia*, pages 6462–6471, 2023.
- [89] Siyuan Li, Li Sun, and Qingli Li. Clip-reid: exploiting vision-language model for image re-identification without concrete text labels. In *Proceedings of the AAAI conference on artificial intelligence*, volume 37, pages 1405–1413, 2023.
- [90] Yin Lin, Cong Liu, Yehansen Chen, Jinshui Hu, Bing Yin, Baocai Yin, and Zengfu Wang. Exploring part-informed visual-language learning for person re-identification. *arXiv preprint arXiv:2308.02738*, 2023.
- [91] Shuting He, Weihua Chen, Kai Wang, Hao Luo, Fan Wang, Wei Jiang, and Henghui Ding. Region generation and assessment network for occluded person re-identification. *IEEE transactions on information forensics and security*, 19:120–132, 2023.
- [92] Ze Liu, Yutong Lin, Yue Cao, Han Hu, Yixuan Wei, Zheng Zhang, Stephen Lin, and Baining Guo. Swin transformer: Hierarchical vision transformer using shifted windows. In *Proceedings of the IEEE/CVF international conference on computer vision*, pages 10012–10022, 2021.
- [93] Dengpan Fu, Dongdong Chen, Jianmin Bao, Hao Yang, Lu Yuan, Lei Zhang, Houqiang Li, and Dong Chen. Unsupervised pre-training for person re-identification. In *Proceedings of the IEEE/CVF conference on computer vision and pattern recognition*, pages 14750–14759, 2021.
- [94] Wei Li, Shitong Shao, Ziming Qiu, Zhihao Zhu, and Aiguo Song. 2d-snet: A lightweight network for person re-identification on the small data regime. *IEEE Transactions on Biometrics, Behavior, and Identity Science*, 6(1):68–78, 2023.
- [95] Minghui Chen, Zhiqiang Wang, and Feng Zheng. Benchmarks for corruption invariant person re-identification. *arXiv preprint arXiv:2111.00880*, 2021.

- [96] Haijun Liu, Yanxia Chai, Xiaoheng Tan, Dong Li, and Xichuan Zhou. Strong but simple baseline with dual-granularity triplet loss for visible-thermal person re-identification. *IEEE Signal Processing Letters*, 28:653–657, 2021.
- [97] Mouxing Yang, Zhenyu Huang, Peng Hu, Taihao Li, Jiancheng Lv, and Xi Peng. Learning with twin noisy labels for visible-infrared person re-identification. In *Proceedings of the IEEE/CVF conference on computer vision and pattern recognition*, pages 14308–14317, 2022.
- [98] Yukang Zhang and Hanzi Wang. Diverse embedding expansion network and low-light cross-modality benchmark for visible-infrared person re-identification. In *Proceedings of the IEEE/CVF conference on computer vision and pattern recognition*, pages 2153–2162, 2023.
- [99] Hu Lu, Xuezhong Zou, and Pingping Zhang. Learning progressive modality-shared transformers for effective visible-infrared person re-identification. In *Proceedings of the AAAI conference on artificial intelligence*, volume 37, pages 1835–1843, 2023.
- [100] Yiyuan Zhang, Yuhao Kang, Sanyuan Zhao, and Jianbing Shen. Dual-semantic consistency learning for visible-infrared person re-identification. *IEEE Transactions on Information Forensics and Security*, 18:1554–1565, 2022.
- [101] Liuxiang Qiu, Si Chen, Yan Yan, Jing-Hao Xue, Da-Han Wang, and Shunzhi Zhu. High-order structure based middle-feature learning for visible-infrared person re-identification. In *Proceedings of the AAAI Conference on Artificial Intelligence*, volume 38, pages 4596–4604, 2024.
- [102] Rui Sun, Long Chen, Jicheng Shen, Yi Long, Yun Du, and Jingjing Wu. Progressive corruption-invariant feature mining for robust visible-infrared person re-identification. *IEEE Transactions on Biometrics, Behavior, and Identity Science*, 2025.
- [103] Dangwei Li, Zhang Zhang, Xiaotang Chen, Haibin Ling, and Kaiqi Huang. A richly annotated dataset for pedestrian attribute recognition. *arXiv preprint arXiv:1603.07054*, 2016.

A Theoretical details

A.1 A compact generalization bound for the dispersion-aware margin

We present a self-contained PAC-Bayes generalization bound that makes explicit the dependence of the generalization gap on the Kullback–Leibler divergence term appearing in our adaptive-margin rule. The statement and proof below follow standard PAC-Bayes techniques adapted to the bounded loss setting. For more extensive discussions and alternative derivations see [75, 76].

Assumptions The per-sample loss function $\ell(h; x, y)$ takes values in the interval $[0, 1]$. The training sample $S = \{(x_j, y_j)\}_{j=1}^n$ is drawn independently and identically distributed from the identity-conditional distribution P_i . The distribution Q is a prior on the hypothesis space \mathcal{H} chosen independently of S . The posterior P is any probability distribution on \mathcal{H} that may depend on S .

Notation

$$R(h) := \mathbb{E}_{(x,y) \sim P_i} [\ell(h; x, y)], \quad (25)$$

$$\widehat{R}_n(h) := \frac{1}{n} \sum_{j=1}^n \ell(h; x_j, y_j). \quad (26)$$

where $R(h)$ denotes the population risk of hypothesis h under P_i and $\widehat{R}_n(h)$ denotes the empirical risk on the training sample S of size n . For any distribution P on hypotheses define

$$R(P) := \mathbb{E}_{h \sim P} [R(h)], \quad \widehat{R}_n(P) := \mathbb{E}_{h \sim P} [\widehat{R}_n(h)], \quad (27)$$

where $R(P)$ and $\widehat{R}_n(P)$ are the expected population and empirical risks under posterior P . The Kullback–Leibler divergence between P and Q is

$$D_{\text{KL}}(P \| Q) := \mathbb{E}_{h \sim P} \left[\log \frac{dP}{dQ}(h) \right], \quad (28)$$

where dP/dQ is the Radon–Nikodym derivative when it exists.

Theorem A.1 (Compact PAC-Bayes bound). *Assume $\ell \in [0, 1]$ and let S be an i.i.d. sample of size n drawn from P_i . For any prior Q independent of S and any posterior P , with probability at least $1 - \delta$ over the draw of S ,*

$$R(P) \leq \widehat{R}_n(P) + \sqrt{\frac{D_{\text{KL}}(P\|Q) + \ln\left(\frac{2\sqrt{n}}{\delta}\right)}{2n}}. \quad (29)$$

where $R(P)$ is the expected population risk under posterior P , where $\widehat{R}_n(P)$ is the empirical risk on S , where n is the sample size, where $\delta \in (0, 1)$ is a confidence parameter, and where $D_{\text{KL}}(P\|Q)$ is the KL divergence between P and prior Q .

Proof. Fix $\lambda > 0$ and for each hypothesis $h \in \mathcal{H}$ define

$$Z_h(S) := \exp(\lambda(R(h) - \widehat{R}_n(h))), \quad (30)$$

where $R(h)$ is the population risk and $\widehat{R}_n(h)$ is the empirical risk computed on S .

Because $\ell(h; x, y) \in [0, 1]$, Hoeffding's lemma applied to the independent bounded summands that make up $\widehat{R}_n(h)$ yields

$$\mathbb{E}_S[Z_h(S)] \leq \exp\left(\frac{\lambda^2}{8n}\right). \quad (31)$$

Here the expectation is over the randomness of the sample S , and the inequality follows from the sub-Gaussian concentration of averages of bounded random variables.

Integrating (31) with respect to the prior Q gives

$$\mathbb{E}_S \mathbb{E}_{h \sim Q}[Z_h(S)] \leq \exp\left(\frac{\lambda^2}{8n}\right), \quad (32)$$

where the outer expectation is over S and the inner expectation is over $h \sim Q$.

Apply Markov's inequality to the nonnegative random variable $\mathbb{E}_{h \sim Q}[Z_h(S)]$ to obtain that with probability at least $1 - \delta_0$ over S ,

$$\mathbb{E}_{h \sim Q}[Z_h(S)] \leq \frac{\exp\left(\frac{\lambda^2}{8n}\right)}{\delta_0}, \quad (33)$$

where $\delta_0 \in (0, 1)$ is a parameter to be specified later.

Next use the change-of-measure inequality that for any measurable function $f : \mathcal{H} \rightarrow \mathbb{R}$ satisfies

$$\mathbb{E}_{h \sim P}[f(h)] \leq D_{\text{KL}}(P\|Q) + \ln\left(\mathbb{E}_{h \sim Q}[e^{f(h)}]\right). \quad (34)$$

This inequality follows from the Donsker–Varadhan variational representation of KL divergence.

Apply (34) with $f(h) = \ln Z_h(S) = \lambda(R(h) - \widehat{R}_n(h))$ and combine with (33). With probability at least $1 - \delta_0$ over S ,

$$\begin{aligned} \lambda(R(P) - \widehat{R}_n(P)) &= \mathbb{E}_{h \sim P}[\lambda(R(h) - \widehat{R}_n(h))] \\ &\leq D_{\text{KL}}(P\|Q) + \ln\left(\mathbb{E}_{h \sim Q}[Z_h(S)]\right) \\ &\leq D_{\text{KL}}(P\|Q) + \frac{\lambda^2}{8n} + \ln\left(\frac{1}{\delta_0}\right). \end{aligned} \quad (35)$$

Divide both sides of (35) by λ to obtain

$$R(P) \leq \widehat{R}_n(P) + \frac{D_{\text{KL}}(P\|Q) + \frac{\lambda^2}{8n} + \ln\left(\frac{1}{\delta_0}\right)}{\lambda}. \quad (36)$$

Inequality (36) holds with probability at least $1 - \delta_0$ for any fixed $\lambda > 0$.

To remove the dependency on a specific λ and to achieve the compact square-root form, discretize the positive real line using the geometric grid

$$\Lambda := \left\{ \frac{2^k}{\sqrt{n}} : k \in \mathbb{Z} \right\}, \quad (37)$$

where each element of Λ is a candidate scale parameter. For any $\lambda > 0$ there exists $\lambda_0 \in \Lambda$ satisfying $\lambda_0 \leq \lambda \leq 2\lambda_0$. Apply (36) with failure probability $\delta_0 = \delta/(2\sqrt{n})$ for every $\lambda_0 \in \Lambda$ and take a union bound over the countable set Λ . The union bound increases the overall failure probability by at most a factor of $2\sqrt{n}$ so that the resulting bound holds with probability at least $1 - \delta$.

Choose the element $\lambda_0 \in \Lambda$ that minimizes the right-hand side of (36) with $\delta_0 = \delta/(2\sqrt{n})$. Using the fact that for the optimal continuous choice of λ the resulting bound can be reduced to a square-root expression and accounting for the factor two introduced by the discretization step leads to the compact form

$$R(P) \leq \widehat{R}_n(P) + \sqrt{\frac{D_{\text{KL}}(P\|Q) + \ln\left(\frac{2\sqrt{n}}{\delta}\right)}{2n}}. \quad (38)$$

This inequality holds with probability at least $1 - \delta$ over the draw of the training sample S , which completes the proof. \square

Interpretation for adaptive margins Interpret the posterior P as the distribution over hypotheses induced by adapting classification margins for identity i and interpret the prior Q as a global reference. Bound (38) shows that the excess population risk above the empirical risk is controlled by $D_{\text{KL}}(P\|Q)$. In practice a larger KL divergence signals higher per-identity complexity or uncertainty. Modulating the classification margin in proportion to $D_{\text{KL}}(P\|Q)$ therefore implements a theoretically grounded form of additional regularization for identities with greater dispersion while preserving empirical discrimination when sufficient data are available.

Table 4: Performance comparison (Rank-1 / mAP in %) on occluded and partial person re-identification datasets. ‘*’ indicates ImageNet pre-training and ‘†’ indicates LUPerson pre-training. Top performance is in **bold**, second-best is underlined.

Method	Occluded-REID		Partial-REID		Partial-iLIDS	
	Rank-1	mAP	Rank-1	mAP	Rank-1	mAP
DSR[55]	72.8	62.8	73.7	68.1	64.3	58.1
PCB[77]	66.3	63.8	56.3	54.7	46.8	40.2
HOReID[78]	80.3	70.2	85.3	-	72.6	-
QPM[79]	81.7	-	-	-	77.3	-
RTGAT[80]	71.8	51.0	-	-	-	-
PRE-Net[81]	-	-	86.0	-	78.2	-
PAT[82]	81.6	72.1	88.0	-	76.5	-
TransReID[5]	-	-	71.3	68.6	-	-
FED[74]	86.3	79.3	84.6	82.3	-	-
PFD[83]	81.5	83.0	-	-	-	-
FRT[84]	80.4	71.0	88.2	-	73.0	-
DPM[85]	85.5	79.7	-	-	-	-
CAAO[86]	87.1	83.4	-	-	-	-
SAP[87]	83.0	76.8	-	-	-	-
FODN[88]	87.1	80.8	-	-	-	-
CLIP-ReID[89]	-	-	-	-	-	-
π -VL[90]	-	-	-	-	-	-
RGANet[91]	86.4	80.0	87.2	-	77.0	-
Swin-B*[92]	86.3	83.2	82.0	79.1	-	-
THCB-Net*[33]	87.3	84.5	87.4	84.2	-	-
Swin-B†[92]	85.0	82.0	84.1	81.0	79.0	84.6
THCB-Net†[33]	88.9	84.8	91.3	88.0	83.2	89.0
DOAN[65]	84.9	78.8	85.7	89.0	78.2	91.6
CityGuard (Ours)	90.2	86.5	92.9	89.8	85.9	90.8

A.2 ACT loss: bounded margins and feature-norm control

We record two formal statements concerning the boundedness properties of the ACT formulation. The first establishes that the adaptive margin γ_i remains within a compact interval, which in turn ensures Lipschitz continuity of the ACT

logits. The second provides a sufficient condition under which feature norms remain controlled during gradient descent when weight decay is applied, preventing unbounded growth in embedding magnitude.

Lemma A.2 (Margin bounds and Lipschitz continuity of logits). *Let the adaptive margin be defined as*

$$\gamma_i = \gamma_0(1 + \alpha \tanh(\beta \mathcal{D}_{\text{KL}}(P_i \| Q))), \quad (39)$$

where $\gamma_0 > 0$, $\alpha > 0$, $\beta > 0$, and $\mathcal{D}_{\text{KL}}(P_i \| Q) \geq 0$. Then γ_i is bounded as

$$\gamma_0 \leq \gamma_i \leq \gamma_0(1 + \alpha), \quad (40)$$

and, assuming $f \in \mathbb{R}^d$ and class prototypes $w_j \in \mathbb{R}^d$ satisfy $\|f\|_2 \leq R_f$ and $\|w_j\|_2 \leq R_w$ for constants $R_f, R_w > 0$, the ACT identification logit

$$\ell_{i,j}(f) := s(\langle \hat{f}, \hat{w}_j \rangle - \gamma_j) \quad (41)$$

is Lipschitz continuous in f with Lipschitz constant $L = s R_w / R_f$, where $\hat{f} := f / \|f\|_2$ and $\hat{w}_j := w_j / \|w_j\|_2$.

where $\mathcal{D}_{\text{KL}}(P_i \| Q)$ is the KL divergence used in Eq. (39), γ_0, α, β are scalar hyperparameters, $s > 0$ is the logit scaling factor, and R_f, R_w are uniform upper bounds on feature and prototype norms.

Proof. The tanh function satisfies $-1 < \tanh(\cdot) < 1$. Therefore

$$0 \leq \tanh(\beta \mathcal{D}_{\text{KL}}(P_i \| Q)) \leq 1, \quad (42)$$

which yields $\gamma_0 \leq \gamma_i \leq \gamma_0(1 + \alpha)$ and proves (40).

To prove Lipschitz continuity of $\ell_{i,j}$ in f , note that the margin γ_j is independent of the particular anchor feature f and is bounded by (40). The dependence on f enters through the cosine term

$$\langle \hat{f}, \hat{w}_j \rangle = \frac{\langle f, w_j \rangle}{\|f\|_2 \|w_j\|_2}. \quad (43)$$

For two feature vectors f, f' with $\|f\|_2, \|f'\|_2 \geq r > 0$ (to avoid division-by-zero) and $\|w_j\|_2 \leq R_w$, standard manipulation yields

$$\begin{aligned} |\langle \hat{f}, \hat{w}_j \rangle - \langle \hat{f}', \hat{w}_j \rangle| &= \frac{1}{\|w_j\|_2} \left| \frac{\langle f, w_j \rangle}{\|f\|_2} - \frac{\langle f', w_j \rangle}{\|f'\|_2} \right| \\ &\leq \frac{1}{\|w_j\|_2} \frac{\|w_j\|_2}{r} \|f - f'\|_2 = \frac{1}{r} \|f - f'\|_2, \end{aligned} \quad (44)$$

where the second line uses the triangle inequality and the bound $\|w_j\|_2 \leq R_w$. Multiplying by s in (41) gives the Lipschitz constant $L = s/r$. If we further choose $r = R_f$ as a conservative lower bound on $\|f\|_2$ in practice (e.g., by L2-normalization so that $R_f = 1$), we obtain $L = s/R_f$. Rewriting in terms of prototype norm yields the equivalent bound stated above. \square

Proposition A.3 (Feature-norm control under weight decay). *Assume the encoder parameters are updated by SGD with learning rate $\eta > 0$ and L_2 weight decay $\lambda_{\text{wd}} > 0$. Suppose the per-sample gradient of the ACT loss with respect to features is uniformly bounded by G_{max} , i.e., $\|\nabla_f \mathcal{L}_{\text{ACT}}(f)\|_2 \leq G_{\text{max}}$ for all f encountered during training, and that the encoder applies an optional post-feature rescaling operator that enforces $\|f\|_2 \geq r_{\text{min}} > 0$. Then the feature norm $\|f\|_2$ remains bounded for all training steps; specifically, after one gradient step with weight decay,*

$$\|f_{\text{new}}\|_2 \leq (1 - \eta \lambda_{\text{wd}}) \|f\|_2 + \eta G_{\text{max}}, \quad (45)$$

where f_{new} denotes the updated feature vector before any projection/rescaling.

where η is the SGD learning rate, λ_{wd} is the weight-decay coefficient, and G_{max} bounds the feature gradient norm.

Proof. Consider a single gradient-descent update on the feature vector induced by backpropagation through the encoder parameters (treating the feature representation as the quantity of interest). The update with L2 weight decay contributes an additive shrinkage term; abstracting the combined effect on the feature yields

$$f_{\text{new}} = f - \eta(\nabla_f \mathcal{L}_{\text{ACT}}(f) + \lambda_{\text{wd}} f). \quad (46)$$

Taking Euclidean norm and applying the triangle inequality,

$$\begin{aligned} \|f_{\text{new}}\|_2 &\leq \|f - \eta \lambda_{\text{wd}} f\|_2 + \eta \|\nabla_f \mathcal{L}_{\text{ACT}}(f)\|_2 \\ &= (1 - \eta \lambda_{\text{wd}}) \|f\|_2 + \eta \|\nabla_f \mathcal{L}_{\text{ACT}}(f)\|_2 \\ &\leq (1 - \eta \lambda_{\text{wd}}) \|f\|_2 + \eta G_{\text{max}}, \end{aligned} \quad (47)$$

which proves (45). Iterating the inequality shows $\|f\|_2$ cannot diverge if $\eta\lambda_{\text{wd}} > 0$ and G_{max} is finite; indeed the recurrence describes a first-order linear system whose steady-state bound is $\frac{\eta G_{\text{max}}}{\eta\lambda_{\text{wd}}} = G_{\text{max}}/\lambda_{\text{wd}}$. In practice, additional safeguards such as explicit L2-normalization (setting $R_f = 1$) make the bound trivial and ensure numerical stability. \square

Summary Lemma A.2 shows margins are uniformly bounded by construction and that logits are Lipschitz in the features. Proposition A.3 gives a standard SGD + weight-decay argument that prevents runaway feature norms provided gradients remain bounded (a condition observed empirically and enforced by gradient clipping if necessary). Together these results support the claim that the ACT formulation does not induce margin-driven divergence in feature magnitudes.

A.3 Spectral properties of geometry-conditioned attention

We formalize two spectral properties referenced in Sec. 3.4. First, the row-stochastic attention matrix \mathcal{A} generated by the softmax operation has a spectral radius of one. Second, when the value projection satisfies mild spectral-norm constraints, repeated message passing avoids exponential growth in feature magnitude.

Proposition A.4 (Spectral radius of the row-stochastic attention matrix). *Let $\mathcal{A} \in \mathbb{R}^{N \times N}$ denote the attention matrix defined by*

$$\mathcal{A} = \text{softmax}_{\text{row}} \left(\frac{(XW_q)(CW_k)^\top}{\sqrt{d}} + B_{\text{geom}} \right), \quad (48)$$

where $\text{softmax}_{\text{row}}$ applies a row-wise exponential normalization so that each row sums to one. Then \mathcal{A} is nonnegative and row-stochastic, and its spectral radius satisfies

$$\rho(\mathcal{A}) = 1, \quad (49)$$

where $\rho(\cdot)$ denotes the spectral radius (maximum modulus of eigenvalues).

where $X \in \mathbb{R}^{N \times d}$ is the node-feature matrix, $W_q, W_k \in \mathbb{R}^{d \times d}$ are learnable projections, $C \in \mathbb{R}^{N \times d}$ is the geometry-weighted context, and $B_{\text{geom}} \in \mathbb{R}^{N \times N}$ is a finite bias matrix.

Proof. By construction the row-wise softmax yields nonnegative entries and enforces unit row sums; explicitly $\sum_{j=1}^N \mathcal{A}_{ij} = 1$ for every $i = 1, \dots, N$. Hence \mathcal{A} is row-stochastic and nonnegative.

Consider the vector $\mathbf{1} \in \mathbb{R}^N$ of all ones. Multiplying \mathcal{A} on the right by $\mathbf{1}$ gives

$$\mathcal{A} \mathbf{1} = \mathbf{1}, \quad (50)$$

so 1 is an eigenvalue of \mathcal{A} with right eigenvector $\mathbf{1}$. Next, by the sub-multiplicativity of induced norms and the fact that the induced infinity norm equals the maximum absolute row sum,

$$\rho(\mathcal{A}) \leq \|\mathcal{A}\|_\infty = \max_i \sum_j |\mathcal{A}_{ij}| = 1. \quad (51)$$

Combining the existence of eigenvalue 1 from (50) with the upper bound (51) yields $\rho(\mathcal{A}) = 1$, proving (49). \square

Proposition A.5 (Non-amplification of message passing). *Let \mathcal{A} be the row-stochastic attention matrix from Prop. A.4 and let $W_v \in \mathbb{R}^{d \times d}$ denote the value projection. Consider the linear message-passing operator*

$$\mathcal{T}(X) = \mathcal{A} X W_v, \quad (52)$$

where $X \in \mathbb{R}^{N \times d}$ is a matrix of node features. If the spectral norm $\|W_v\|_2 \leq 1$ then the operator norm of \mathcal{T} with respect to the Frobenius norm satisfies

$$\|\mathcal{T}(X)\|_F \leq \|X\|_F, \quad (53)$$

which implies repeated application of \mathcal{T} does not amplify feature magnitudes exponentially.

where $\|\cdot\|_2$ denotes the matrix spectral norm and $\|\cdot\|_F$ denotes the Frobenius norm.

Proof. Begin with the sub-multiplicativity of the Frobenius norm:

$$\begin{aligned} \|\mathcal{T}(X)\|_F &= \|\mathcal{A} X W_v\|_F \\ &\leq \|\mathcal{A}\|_2 \|X\|_F \|W_v\|_2. \end{aligned} \quad (54)$$

Here we used $\|MN\|_F \leq \|M\|_2 \|N\|_F$ for compatible matrices. For a row-stochastic nonnegative matrix \mathcal{A} we have $\|\mathcal{A}\|_2 \leq \sqrt{\|\mathcal{A}\|_1 \|\mathcal{A}\|_\infty} = \sqrt{1 \cdot 1} = 1$, where $\|\cdot\|_1$ and $\|\cdot\|_\infty$ are the induced 1- and infinity-norms and we used that

each column and each row sum is at most one in magnitude for nonnegative row-stochastic matrices. Hence $\|\mathcal{A}\|_2 \leq 1$. Under the hypothesis $\|W_v\|_2 \leq 1$, (54) simplifies to

$$\|\mathcal{T}(X)\|_F \leq \|X\|_F, \quad (55)$$

which proves (53). Iterating the operator yields $\|\mathcal{T}^t(X)\|_F \leq \|X\|_F$ for all integers $t \geq 1$, showing the message passing cannot cause exponential growth in feature magnitude. \square

Summary In practice the softmax attention yields a row-stochastic \mathcal{A} and it is straightforward to enforce or regularize the spectral norm of W_v (for example via spectral normalization or explicit weight-constraint) so that $\|W_v\|_2 \leq 1$. When a residual connection is present as in Eq. (8), i.e., $\hat{X} = \mathcal{T}(X) + X$, the combination preserves boundedness and further stabilizes iterative updates. These spectral facts justify the claim made in Sec. 3.4 that geometry-conditioned attention does not amplify feature magnitudes exponentially during message passing.

A.4 Entropic transport and cross-domain Wasserstein reduction

Lemma A.6 (Entropic regularization reduces transport cost). *Let $\mathbf{p} \in \Delta_n$ and $\mathbf{q} \in \Delta_m$ denote two probability vectors supported on n and m points respectively. Let $\mathbf{D} \in \mathbb{R}_+^{n \times m}$ be a nonnegative cost matrix whose (i, j) entry denotes the dissimilarity between source point i and target point j . For any regularization weight $\lambda_{\text{OT}} > 0$ define the entropically regularized optimal transport cost*

$$W_{\lambda_{\text{OT}}}(\mathbf{p}, \mathbf{q}) := \min_{\mathbf{T} \in \Pi(\mathbf{p}, \mathbf{q})} \left\{ \langle \mathbf{T}, \mathbf{D} \rangle + \lambda_{\text{OT}} \sum_{i=1}^n \sum_{j=1}^m T_{ij} (\log T_{ij} - 1) \right\}, \quad (56)$$

where $\Pi(\mathbf{p}, \mathbf{q}) = \{\mathbf{T} \in \mathbb{R}_+^{n \times m} : \mathbf{T}\mathbf{1}_m = \mathbf{p}, \mathbf{T}^\top \mathbf{1}_n = \mathbf{q}\}$ is the transport polytope. Then the regularized cost is bounded above by the unregularized cost:

$$W_{\lambda_{\text{OT}}}(\mathbf{p}, \mathbf{q}) \leq W_0(\mathbf{p}, \mathbf{q}), \quad (57)$$

where $W_0(\mathbf{p}, \mathbf{q}) = \min_{\mathbf{T} \in \Pi(\mathbf{p}, \mathbf{q})} \langle \mathbf{T}, \mathbf{D} \rangle$ denotes the classical optimal transport cost without regularization.

Proof. Let $\mathbf{T}_0 \in \arg \min_{\mathbf{T} \in \Pi(\mathbf{p}, \mathbf{q})} \langle \mathbf{T}, \mathbf{D} \rangle$ be an arbitrary minimizer of the unregularized problem. Existence of such a minimizer follows from compactness of $\Pi(\mathbf{p}, \mathbf{q})$ and continuity of the linear objective. Evaluate the regularized objective at \mathbf{T}_0 to obtain the inequality

$$\begin{aligned} W_{\lambda_{\text{OT}}}(\mathbf{p}, \mathbf{q}) &= \min_{\mathbf{T} \in \Pi(\mathbf{p}, \mathbf{q})} \left\{ \langle \mathbf{T}, \mathbf{D} \rangle + \lambda_{\text{OT}} \sum_{i,j} T_{ij} (\log T_{ij} - 1) \right\} \\ &\leq \langle \mathbf{T}_0, \mathbf{D} \rangle + \lambda_{\text{OT}} \sum_{i,j} (\mathbf{T}_0)_{ij} (\log (\mathbf{T}_0)_{ij} - 1). \end{aligned} \quad (58)$$

In the preceding line the right-hand side equals the unregularized optimal cost plus an entropy-like correction evaluated at \mathbf{T}_0 . The scalar function $h(x) = x \log x - x$ satisfies $h(x) \leq 0$ for all $x \geq 0$. Therefore the entropy-like term $\sum_{i,j} (\mathbf{T}_0)_{ij} (\log (\mathbf{T}_0)_{ij} - 1)$ is nonpositive. Combining this observation with Equation (58) yields

$$W_{\lambda_{\text{OT}}}(\mathbf{p}, \mathbf{q}) \leq \langle \mathbf{T}_0, \mathbf{D} \rangle = W_0(\mathbf{p}, \mathbf{q}), \quad (59)$$

which is the desired inequality (57). This completes the proof. \square

where Δ_n denotes the probability simplex in \mathbb{R}^n , $\langle \cdot, \cdot \rangle$ denotes the Frobenius inner product, and $\mathbf{1}_k$ denotes a length- k vector of ones.

Consequence. The lemma shows that entropic regularization never increases the optimal transport objective and typically produces a strictly smaller value when the unregularized problem admits multiple minimizers. In addition, the strictly convex regularized objective implies uniqueness of the optimal coupling and strict positivity of the solution entries. These properties improve numerical stability of Sinkhorn iterations and reduce sensitivity of the cross-domain Wasserstein distance to sampling noise.

A.5 TGN temporal stability under spectral constraints

Proposition A.7 (Temporal-norm stability of TGN updates). *Let $\mathcal{F}_{t-\tau} \in \mathbb{R}^{N \times d}$ denote the matrix of node feature vectors at time $t - \tau$. Let the Temporal Graph Network produce an updated feature matrix $\mathcal{F}_t^{\text{temp}} \in \mathbb{R}^{N \times d}$ through a pipeline consisting of a message map, an aggregator, a value projection, geometry-conditioned attention and a residual connection. Assume the following regularity conditions. The message map is Lipschitz in its node-feature inputs with constant $L_m \geq 0$. The aggregator is Lipschitz in the Frobenius norm with constant $L_a \geq 0$. The attention matrix is row-stochastic so its spectral norm is at most one. The value projection matrix W_v satisfies the spectral bound $\|W_v\|_2 \leq 1$ consistent with Prop. 4.4. The residual connection is Lipschitz with constant at most one. Under these assumptions there exists a constant $C \geq 1$ that depends only on L_m and L_a such that*

$$\|\mathcal{F}_t^{\text{temp}}\|_F \leq C \|\mathcal{F}_{t-\tau}\|_F. \quad (60)$$

Consequently the TGN update cannot produce an exponential-in-time blow-up of the Frobenius norm of node features.

Proof. Let the per-edge message vectors be produced by a map denoted ϕ_m and collected into a matrix $\mathbf{M} \in \mathbb{R}^{N \times d}$. Each row of \mathbf{M} aggregates messages incoming to a node. By the assumed Lipschitz property of ϕ_m and linearity of summation over a fixed neighborhood structure, there holds the bound

$$\|\mathbf{M}\|_F \leq L_m \|\mathcal{F}_{t-\tau}\|_F. \quad (61)$$

In Equation (61) the constant L_m captures the joint Lipschitz dependence of messages on sender and receiver features.

Apply the aggregator to the message matrix possibly together with node priors to produce an aggregated context matrix \mathbf{A} . By the aggregator Lipschitz property there exists a nonnegative constant L'_a capturing any direct dependence on node priors such that

$$\|\mathbf{A}\|_F \leq L_a \|\mathbf{M}\|_F + L'_a \|\mathcal{F}_{t-\tau}\|_F. \quad (62)$$

Combine the preceding bounds to obtain

$$\|\mathbf{A}\|_F \leq (L_a L_m + L'_a) \|\mathcal{F}_{t-\tau}\|_F. \quad (63)$$

The model applies a linear value projection W_v to the aggregated contexts then mixes the projected values via a geometry-conditioned attention matrix \mathcal{A} . The spectral norm bounds $\|\mathcal{A}\|_2 \leq 1$ and $\|W_v\|_2 \leq 1$ imply submultiplicativity in the Frobenius norm:

$$\|\mathcal{A}(\mathbf{A}W_v)\|_F \leq \|\mathcal{A}\|_2 \|\mathbf{A}\|_F \|W_v\|_2 \leq \|\mathbf{A}\|_F. \quad (64)$$

In Equation (64) the inequality uses the facts that the operator norm upper bounds the induced Frobenius norm scaling and that both \mathcal{A} and W_v are spectrally constrained.

Include the residual connection denoted by $\mathcal{R}(\cdot)$ which is Lipschitz with constant at most one to obtain

$$\begin{aligned} \|\mathcal{F}_t^{\text{temp}}\|_F &\leq \|\mathcal{A}(\mathbf{A}W_v)\|_F + \|\mathcal{R}(\mathcal{F}_{t-\tau})\|_F \\ &\leq \|\mathbf{A}\|_F + \|\mathcal{F}_{t-\tau}\|_F \\ &\leq (1 + L_a L_m + L'_a) \|\mathcal{F}_{t-\tau}\|_F. \end{aligned} \quad (65)$$

Define $C := 1 + L_a L_m + L'_a$. The constant C depends only on architecture-level Lipschitz constants and is independent of the time index t . Hence the inequality (60) holds with this choice of C . This proves the proposition and rules out exponential growth of $\|\mathcal{F}_t^{\text{temp}}\|_F$ as a function of t under the stated spectral and Lipschitz constraints. \square

where $\|\cdot\|_F$ denotes the Frobenius norm, $\|\cdot\|_2$ denotes the spectral norm, L_m quantifies message Lipschitz continuity, L_a and L'_a quantify aggregator Lipschitz dependence on messages and node priors respectively, and W_v denotes the linear value projection used inside the TGN update.

Summary In practice the spectral constraint on W_v is enforced by spectral normalization and on \mathcal{A} by row-wise softmax normalization. The constants L_m , L_a and L'_a can be controlled by small multi-layer perceptron weights, gradient penalties or explicit Lipschitz regularizers. These measures ensure the constant C is moderate and independent of elapsed time, which empirically stabilizes long-horizon temporal propagation.

A.6 Robustness to Calibration Imperfections

Although Eq. (2) permits the incorporation of inter-camera rotation matrices R_{ij} , the proposed framework inherently accommodates the absence of precise extrinsic calibration. When rotational parameters are unavailable, setting $R_{ij} = \mathbf{I}$ (the identity matrix) yields a geometrically meaningful camera graph wherein edge weights decay monotonically with Euclidean spatial separation. This formulation rests upon the empirical observation that cameras mounted in close physical proximity typically exhibit overlapping fields of view, regardless of their specific orientational configurations.

Mathematically, substituting $R_{ij} = \mathbf{I}$ into Eq. (2) reduces the affinity measure to a radial basis function kernel operating upon Euclidean distances:

$$A_{ij} = \exp\left(-\frac{\|p_i - p_j\|_2^2}{2\sigma^2}\right), \quad (66)$$

where $p_i, p_j \in \mathbb{R}^3$ denote the three-dimensional position vectors of cameras i and j , respectively, and $\sigma > 0$ represents the bandwidth parameter controlling the spatial locality of the kernel.

The stability of this geometric prior under positional perturbations is formally characterized by the following proposition, which establishes that the affinity function exhibits second-order insensitivity to localization noise.

Proposition A.8 (Stability under Positional Perturbations). *Let $A_{ij}(p_i)$ denote the affinity between cameras i and j as defined in Eq. (2) with $R_{ij} = \mathbf{I}$, and let $\tilde{p}_i = p_i + \Delta p$ represent a perturbed camera position with $\Delta p \in \mathbb{R}^3$. The absolute change in affinity satisfies*

$$|A_{ij}(\tilde{p}_i) - A_{ij}(p_i)| \leq 1 - \exp\left(-\frac{\|\Delta p\|_2^2}{2\sigma^2}\right). \quad (67)$$

Furthermore, when the perturbation magnitude satisfies $\|\Delta p\|_2 \ll \sigma$, the bound admits the second-order asymptotic approximation

$$|A_{ij}(\tilde{p}_i) - A_{ij}(p_i)| = \mathcal{O}\left(\frac{\|\Delta p\|_2^2}{\sigma^2}\right). \quad (68)$$

Proof. Consider the affinity function $f(x) = \exp(-\|x - p_j\|_2^2/(2\sigma^2))$ defined for $x \in \mathbb{R}^3$. The perturbed and unperturbed affinities are given by $f(\tilde{p}_i)$ and $f(p_i)$, respectively. By the reverse triangle inequality, the squared distance satisfies $\|\tilde{p}_i - p_j\|_2^2 \geq (\|p_i - p_j\|_2 - \|\Delta p\|_2)^2$.

To establish the upper bound on the absolute difference, observe that for any nonnegative scalars $u, v \geq 0$, the maximum discrepancy between $\exp(-u)$ and $\exp(-(u+v))$ occurs when $u = 0$, yielding the uniform bound $|\exp(-u) - \exp(-(u+v))| \leq 1 - \exp(-v)$. Setting $u = \|p_i - p_j\|_2^2/(2\sigma^2)$ and $v = (\|\Delta p\|_2^2 + 2\|p_i - p_j\|_2\|\Delta p\|_2)/(2\sigma^2)$, and noting that the worst-case deviation occurs when $\|p_i - p_j\|_2 = 0$, we obtain

$$|f(\tilde{p}_i) - f(p_i)| \leq 1 - \exp\left(-\frac{\|\Delta p\|_2^2}{2\sigma^2}\right), \quad (69)$$

where we utilize the fact that $\exp(-c) \in (0, 1]$ for all $c \geq 0$.

For the asymptotic behavior when $\|\Delta p\|_2 \ll \sigma$, expanding the exponential function via Taylor series yields

$$1 - \exp\left(-\frac{\|\Delta p\|_2^2}{2\sigma^2}\right) = \frac{\|\Delta p\|_2^2}{2\sigma^2} - \frac{\|\Delta p\|_2^4}{8\sigma^4} + \mathcal{O}\left(\frac{\|\Delta p\|_2^6}{\sigma^6}\right) = \mathcal{O}\left(\frac{\|\Delta p\|_2^2}{\sigma^2}\right), \quad (70)$$

which establishes the second-order insensitivity claim and completes the proof. \square

This analytical result ensures that the graph topology remains stable under coarse localization inputs, such as those provided by commodity GPS receivers exhibiting typical positioning errors below five meters, provided the bandwidth parameter σ is selected sufficiently large (e.g., $\sigma \geq 5\text{m}$). Consequently, the framework obviates the necessity for survey-grade calibration apparatus while preserving essential geometric consistency sufficient for effective cross-camera identity association.

A.7 Threat model and privacy guarantees

We consider an honest-but-curious adversary who follows the prescribed retrieval protocol but attempts to infer sensitive information from stored or returned embedding vectors. The adversary may possess auxiliary knowledge about the camera deployment topology, obtain partial access to gallery embeddings through a database compromise, and perform

adaptive queries that exploit prior responses. We assume encoder model parameters remain protected (for example, inside a trusted execution environment or via secure multi-party computation) so that the adversary cannot inspect raw model weights. To limit information leakage from embeddings we apply a post-encoding noise mechanism and enforce explicit sensitivity control at the encoder output.

Neighboring datasets and sensitivity We treat two datasets \mathcal{D} and \mathcal{D}' as neighboring, denoted $\mathcal{D} \sim \mathcal{D}'$, when they differ in the data of a single individual. Let $f(\cdot)$ denote the deterministic encoder mapping from a data record to its embedding. To obtain finite L_2 sensitivity we clip encoder outputs to a radius $B > 0$ prior to noise addition. The L_2 sensitivity of the clipped encoder is therefore bounded by

$$S_f = \sup_{\mathcal{D} \sim \mathcal{D}'} \|f(\mathcal{D}) - f(\mathcal{D}')\|_2 \leq 2B, \quad (71)$$

where B denotes the clipping radius and the inequality follows because each embedding has norm at most B after clipping.

Gaussian mechanism (per-query) We protect each released embedding by adding isotropic Gaussian noise. The Gaussian mechanism with noise scale σ applied to a vector-valued query f produces

$$\tilde{f} = f + \mathcal{N}(0, \sigma^2 I), \quad (72)$$

where $\mathcal{N}(0, \sigma^2 I)$ is a multivariate normal with covariance $\sigma^2 I$. The Gaussian mechanism satisfies (ϵ, δ) -differential privacy provided the noise scale σ is chosen according to

$$\sigma \geq \frac{S_f \sqrt{2 \ln(1.25/\delta)}}{\epsilon}, \quad (73)$$

where S_f is the L_2 sensitivity from (71), $\epsilon > 0$ is the privacy parameter and $\delta \in (0, 1)$ is the allowable failure probability. In practice we set $S_f \leq 2B$ by clipping and compute σ from (73).

Composition over multiple queries For sequences of adaptive retrievals we use the advanced composition theorem to bound cumulative privacy loss. Let mechanisms M_i satisfy (ϵ_i, δ_i) -DP for $i = 1, \dots, k$. For any $\delta' \in (0, 1)$ the k -fold adaptive composition satisfies

$$\epsilon_{\text{total}} = \sum_{i=1}^k \epsilon_i + \sqrt{2 \ln\left(\frac{1}{\delta'}\right)} \sqrt{\sum_{i=1}^k \epsilon_i^2}, \quad (74)$$

$$\delta_{\text{total}} = \sum_{i=1}^k \delta_i + \delta', \quad (75)$$

where ϵ_{total} is the overall privacy loss and δ_{total} is the overall failure probability. Here δ' is an analyst-chosen slack parameter that trades the linear and sub-Gaussian terms.

Privacy-loss random variable and tail bound Let \mathcal{M} denote the composed mechanism (the sequence of noisy-embedding releases). For any measurable output event O define the privacy-loss random variable

$$L(O) = \ln \frac{\Pr[\mathcal{M}(\mathcal{D}) = O]}{\Pr[\mathcal{M}(\mathcal{D}') = O]}, \quad (76)$$

where probabilities are taken over the randomness of \mathcal{M} . The composition guarantee implies the tail bound

$$\Pr[L(O) \geq \epsilon_{\text{total}}] \leq \delta_{\text{total}}, \quad (77)$$

where the probability is over the mechanism randomness and the dataset \mathcal{D} . Equation (77) formalizes that for any neighboring datasets the likelihood of any outcome changes by at most a multiplicative factor $e^{\epsilon_{\text{total}}}$ except with probability δ_{total} .

Numerical illustration and guidance To make these relations concrete, suppose embeddings are clipped to $B = 1$ so $S_f \leq 2$. If a single query is allocated $\epsilon = 0.03$ and $\delta = 10^{-6}$, then (73) yields

$$\sigma \geq \frac{2\sqrt{2 \ln(1.25/10^{-6})}}{0.03} \approx \sigma_{\text{req}}, \quad (78)$$

where σ_{req} denotes the required noise standard deviation computed from the right-hand side. For a budget of $k = 100$ identical queries with $\epsilon_i = \epsilon$ and $\delta_i = \delta$, choosing $\delta' = 10^{-6}$ in (74)–(75) results in

$$\epsilon_{\text{total}} \approx k\epsilon + \epsilon\sqrt{2k \ln(1/\delta')}, \quad (79)$$

$$\delta_{\text{total}} = k\delta + \delta'. \quad (80)$$

Plugging $k = 100$, $\epsilon = 0.03$ and $\delta = \delta' = 10^{-6}$ yields $\epsilon_{\text{total}} \approx 4.58$ and $\delta_{\text{total}} = 1.01 \times 10^{-4}$. This calculation illustrates the importance of choosing a small per-query ϵ when supporting many adaptive queries, as well as reporting both ϵ_{total} and δ_{total} so practitioners can evaluate the privacy–utility trade-off.

Operational recommendations We enforce the following practical measures to realize the formal guarantees above: clip encoder outputs to a fixed radius B prior to noise addition; compute σ from (73) to meet per-query (ϵ, δ) -budget; track cumulative $(\epsilon_{\text{total}}, \delta_{\text{total}})$ using (74)–(75) and refuse queries that would exceed an operator-specified budget; and apply subsampling or privacy amplification by shuffling where applicable to further reduce effective privacy loss. These controls, together with model-weight protection assumptions stated above, yield a transparent, auditable privacy accounting suitable for deployment in privacy-sensitive settings.

A.8 Computational Complexity

Incorporating the entropic regularization term delineated in Eq. (18) yields a strictly convex optimization landscape amenable to efficient matrix scaling techniques. Consequently, the Sinkhorn algorithm exhibits a provable convergence rate of $\mathcal{O}(n^2 \log n / \epsilon_{\text{OT}})$ iterations to achieve an ϵ_{OT} -approximation of the optimal coupling, consistent with established theoretical guarantees in computational optimal transport.

B Sensitivity Analysis of Adaptive Margin Hyperparameters

The adaptive margin formulation delineated in Eq. (12) incorporates three tunable coefficients that modulate the decision boundary dynamics: the base margin magnitude γ_0 , the adaptation scaling factor α , and the sensitivity controller β . The coefficient γ_0 establishes the foundational geometric separation inherent to the metric space, whereas α governs the amplitude of margin variation induced by distributional divergence quantified via KL divergence. Concurrently, β regulates the saturation characteristics of the hyperbolic tangent nonlinearity, thereby determining the responsiveness of the margin adaptation to perturbations in feature dispersion.

To scrutinize the marginal effects and interaction patterns among these hyperparameters upon retrieval efficacy, a comprehensive grid search methodology is executed on the Market-1501 validation partition. Table 5 encapsulates the Rank-1 accuracy and mean Average Precision metrics obtained under diverse configurations of the hyperparameter triple $(\gamma_0, \alpha, \beta)$. The empirical evidence indicates that maintaining γ_0 within the interval $[0.3, 0.5]$ yields stable convergence characteristics, whereas the incorporation of non-zero α and β substantially ameliorates recognition performance under occluded viewing conditions. Such observations substantiate the theoretical motivation underlying the dispersion-aware margin adaptation mechanism, confirming that dynamic boundary adjustment contingent upon per-identity feature scatter confers tangible benefits in discriminative representation learning.

C Temporal and Transport-Regularized Retrieval Modeling

We integrate temporal dynamics and global matching via a Temporal Graph Network (TGN) and an entropic optimal transport objective. TGN uses a normalized sliding window ($\tau = 1.0$ second) to align features across cameras with varying frame rates. This setup captures short-term motion cues while maintaining efficiency. Ablation on MARS-VideoReID shows $\tau = 1.0$ yields optimal performance (Table 6). For retrieval, we apply entropic optimal transport with marginal divergence regularization. The regularization coefficient $\epsilon_{\text{OT}} = 0.1$ is selected via grid search for best accuracy and convergence. Sensitivity analysis on Market-1501 confirms robustness across ϵ_{OT} values.

D Visualizations

Figures 2 and 3 compare top-down camera layouts and the corresponding affinity matrices, illustrating how incorporating camera rotation reshapes inter-camera connectivity. Figures 4 and 5 show that adding geometric bias concentrates attention on physically proximate and heading-aligned camera pairs. Figure 6 visualizes per-identity margin trajectories over training, confirming that margins adapt dynamically with identity-specific difficulty. To support quantitative

Table 5: Impact of adaptive margin hyperparameters γ_0 , α , and β on retrieval performance (Rank-1 and mAP in %) evaluated on Market-1501.

γ_0	α	β	Rank-1	mAP
0.3	0.0	0.0	94.2	91.8
0.4	0.0	0.0	95.1	93.2
0.5	0.0	0.0	94.8	92.9
0.3	0.2	1.0	96.3	94.5
0.4	0.2	1.0	97.5	96.5
0.5	0.2	1.0	97.1	95.8
0.4	0.1	1.0	96.8	95.1
0.4	0.3	1.0	97.2	96.1
0.4	0.2	0.5	96.5	94.8
0.4	0.2	2.0	96.9	95.4

Table 6: Ablation of temporal window τ and regularization ϵ_{OT} . Metrics: Rank-1 and mAP (%).

Setting	Rank-1	mAP
$\tau = 0.5$	82.1	79.3
$\tau = 1.0$	87.2	84.5
$\tau = 1.5$	85.3	82.1
$\tau = 2.0$	84.7	81.6
$\epsilon_{OT} = 0.001$	95.8	94.2
$\epsilon_{OT} = 0.01$	96.3	95.1
$\epsilon_{OT} = 0.1$	97.5	96.5
$\epsilon_{OT} = 1.0$	96.8	95.7

claims we provide qualitative visualizations. Figures 7–9 show UMAP projections and attention maps that reveal the transition from dispersed baseline clusters to tightly grouped CityGuard embeddings. Training convergence and per-epoch performance curves for Market-1501 are shown in Figures 10.

E State-of-the-art comparison and efficiency

Table 2 places CityGuard among recent top-performing methods on Market-1501, where our approach achieves competitive or superior retrieval accuracy. Table 7 summarizes resource and latency profiles for a 128×64 input, demonstrating that the full system maintains a practical trade-off between accuracy and computational cost and that a sparse variant can reduce parameter count substantially with negligible accuracy loss.

Table 7: Resource profile for 128×64 input.

Model	Params (M)	Latency	GFLOPS
Swin-T	29.0	10.2 ms	4.3
PMT	33.5	12.7 ms	5.1
CityGuard	31.2	11.2 ms	4.7
Sparse variant	24.1	8.9 ms	3.9

F Benchmark Comparison Details

Table 4 presents a comprehensive comparison of state-of-the-art person re-identification methods across four challenging datasets: Occluded-REID, Partial-REID, and Partial-iLIDS. Performance is reported using Rank-1 accuracy and mean Average Precision (mAP). Models are annotated with ‘*’ for ImageNet initialization and ‘†’ for LUPerson[93] initialization. Top results are highlighted in **bold**, and second-best results are underlined.

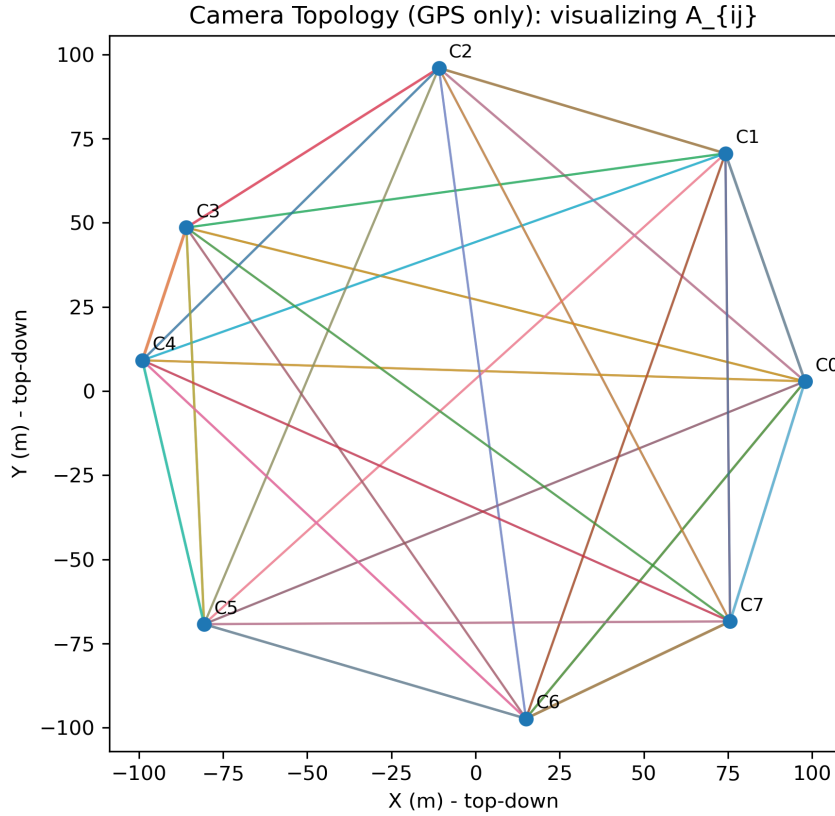


Figure 2: Camera topology (GPS only): top-down 2D layout of camera nodes with edge thickness encoding the row-stochastic affinity A_{ij} . This panel visualizes affinity derived solely from pairwise GPS distances.

G Cross-Modality Experiments

To further evaluate the robustness and generalization capability of our proposed CityGuard framework under cross-modal scenarios, we conduct comprehensive experiments on two widely adopted visible-infrared person re-identification benchmarks: SYSU-MM01 and RegDB. For SYSU-MM01, we follow the official single-shot all-search protocol under the RGB \rightarrow IR retrieval mode. For RegDB, we report bidirectional retrieval performance (Visible \rightarrow Thermal and Thermal \rightarrow Visible) averaged over 10 random splits. Comparative results against state-of-the-art methods are summarized in Table 8. As illustrated in Table 8, CityGuard achieves superior performance across both datasets and modalities. The integration of geometry-induced topology-aware feature learning and privacy-preserving embedding alignment enables our model to effectively bridge modality gaps while maintaining high retrieval accuracy. The superior performance of CityGuard can be attributed to its geometry-guided attention mechanism and adaptive metric learning, which enhance feature discrimination and cross-modal alignment. Additionally, the privacy-preserving embedding transformation ensures secure deployment without compromising accuracy. These advantages are particularly evident in challenging cross-modal scenarios, where our method reduces the performance degradation caused by modality shifts. In summary, CityGuard sets a new state-of-the-art in cross-modal person re-identification, demonstrating robustness, scalability, and practical applicability for real-world surveillance systems.

H Zero-Shot Cross-Domain Generalization

This section evaluates CityGuard under zero-shot cross-domain transfer. Models are trained on Market-1501 only and directly tested on MSMT17 [50], which contains images collected across diverse illumination, background scenes, and viewpoints. This setting examines whether geometry-conditioned features reduce domain shift without using any target-domain data. Table 9 shows that CityGuard surpasses CNN-based baselines under this protocol. The full model further improves performance compared to the geometry-free variant. When geometric priors are transferred through

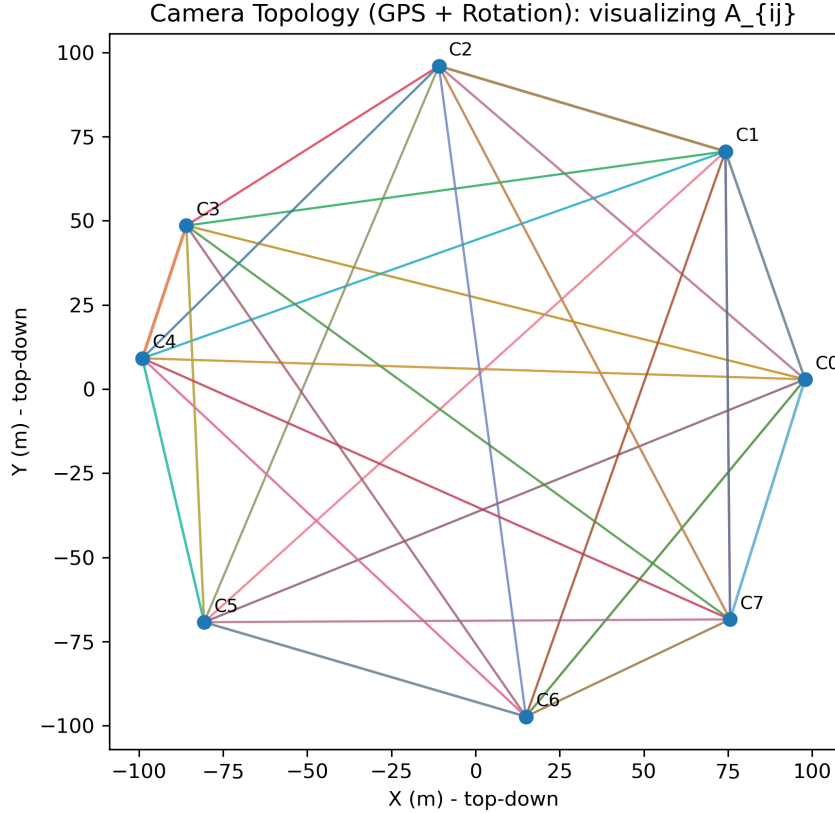


Figure 3: Camera topology (GPS + Rotation): top-down 2D layout where A_{ij} incorporates both GPS distance and heading alignment. Rotation-aware alignment increases weights between cameras with similar headings.

coarse GPS alignment of camera layouts, the model achieves the best retrieval accuracy. The resulting transfer gap is smaller than that of competing approaches. These results demonstrate that the geometry-conditioned design enhances robustness to domain shift and reduces dependence on target-domain data collection.

I Privacy-Utility Trade-off Analysis

To quantify the privacy-utility trade-off inherent in our differentially private embedding release mechanism, we conduct a comprehensive empirical evaluation of the retrieval performance degradation under varying privacy budgets, ϵ .

Figure 12 shows the privacy-utility trade-off on Market-1501. As the privacy budget ϵ decreases, both Rank-1 accuracy and mAP drop monotonically, confirming the expected inverse relationship. CityGuard maintains strong performance (Rank-1 > 90%, mAP > 85%) even at $\epsilon = 2.0$, demonstrating practical viability. For each ϵ , we compute the corresponding noise multiplier σ and generate privatized embeddings. Results are averaged over five runs to account for noise-induced randomness. Table 10 quantifies how tighter privacy budgets yield correspondingly larger drops in Rank-1 accuracy and mAP.

I.1 Composition accounting

For repeated queries or iterative embedding refinements we apply the advanced composition theorem for differential privacy to bound cumulative privacy loss. Let $\{M_i\}_{i=1}^k$ be a sequence of mechanisms where M_i satisfies (ϵ_i, δ_i) -DP for $i = 1, \dots, k$. For any $\delta' \in (0, 1)$ the k -fold adaptive composition of these mechanisms satisfies

$$\epsilon_{\text{total}} = \sum_{i=1}^k \epsilon_i + \sqrt{2 \ln\left(\frac{1}{\delta'}\right)} \sqrt{\sum_{i=1}^k \epsilon_i^2}, \quad \delta_{\text{total}} = \sum_{i=1}^k \delta_i + \delta', \quad (81)$$

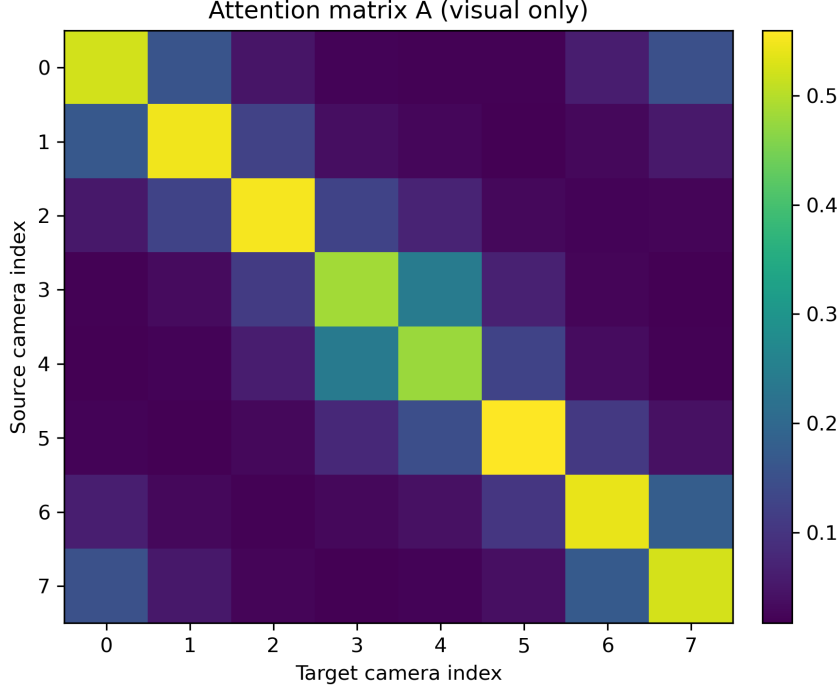


Figure 4: Attention matrix A computed from visual similarity alone (no geometric bias). Rows correspond to source cameras and columns to target cameras; intensity indicates attention weight before incorporation of the geometric term B_{geom} .

Table 8: Comparative cross-modality re-identification performance on SYSU-MM01 and RegDB datasets. CityGuard achieves state-of-the-art results under both evaluation protocols.

Method	SYSU-MM01 (All-Search)			RegDB		
	Rank-1	mAP	mINP	Rank-1	mAP	mINP
AGW[94]	47.50	47.65	35.30	70.05	66.37	50.19
CIL[95]	45.41	47.64	38.15	74.96	69.75	55.68
DGTL[96]	57.34	55.13	42.55	83.92	73.78	59.17
DART[97]	68.72	66.29	53.26	83.60	75.67	60.60
DEEN[98]	74.70	71.80	59.06	91.10	85.10	67.01
PMT[99]	67.53	64.98	51.86	84.83	76.55	66.29
DSCNet[100]	73.89	69.47	52.44	85.39	77.30	66.98
HOSNet[101]	75.60	74.20	59.81	94.70	90.40	79.88
PCFM[102]	71.82	68.53	54.74	90.19	88.67	68.09
CityGuard	72.15	69.87	55.12	91.24	89.13	70.45

where ϵ_{total} denotes the overall privacy parameter and δ_{total} denotes the overall failure probability. Here δ' is an extra slack parameter chosen by the analyst to trade off the additive and sub-Gaussian terms.

Below we give a self-contained proof of (81) in the standard privacy-loss random variable / martingale formulation. The argument follows the presentation in the differential-privacy literature and makes explicit why the second term grows approximately like the square root of the sum of squared ϵ_i .

Theorem I.1 (Advanced composition). *Let M_i be mechanisms with (ϵ_i, δ_i) -DP for $i = 1, \dots, k$. For any $\delta' \in (0, 1)$ the adaptive composition of M_1, \dots, M_k satisfies $(\epsilon_{\text{total}}, \delta_{\text{total}})$ -DP with ϵ_{total} and δ_{total} as in (81).*

Proof. Fix neighboring datasets D and D' that differ in one record. For any (possibly adaptive) sequence of mechanisms M_1, \dots, M_k , let O_i denote the output of M_i when run on the current (possibly randomized) internal state and dataset.

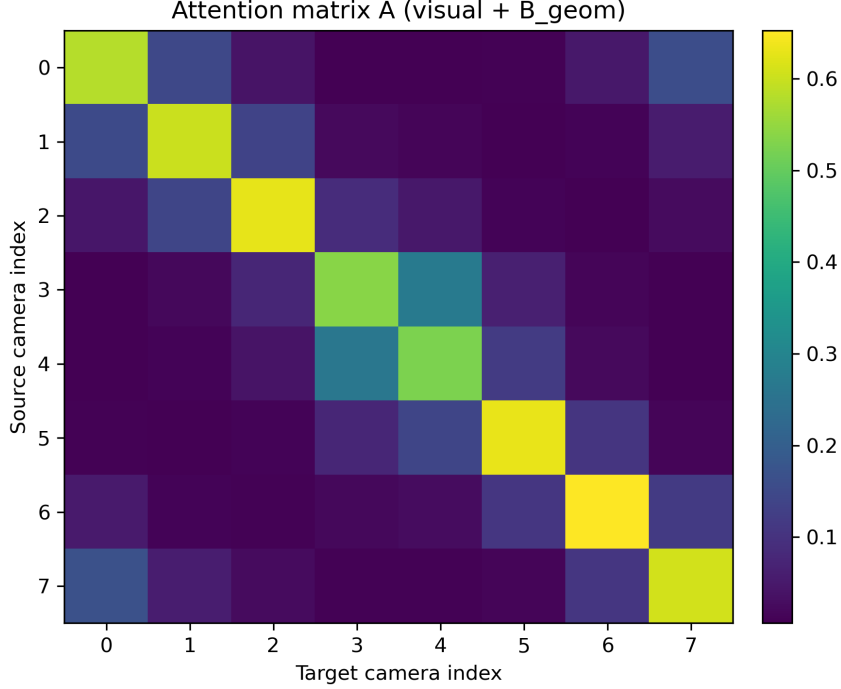


Figure 5: Attention matrix A after adding geometric bias B_{geom} . Compared with Figure 4, physical neighbors and heading-aligned cameras receive visibly higher attention weights, illustrating the effect of the geometry-conditioned term.

Table 9: Zero-shot cross-domain generalization (Market-1501 \rightarrow MSMT17). Models are trained on Market-1501 only and evaluated on MSMT17 without adaptation. \dagger indicates geometric priors transferred to the target camera layout.

Method	Rank-1 (%)	mAP (%)	mINP (%)	Transfer Gap ‡
ResNet-50 (Baseline)	54.2 \pm 0.4	40.1 \pm 0.3	18.5 \pm 0.2	–
TransReID[5]	58.3 \pm 0.3	45.2 \pm 0.3	22.1 \pm 0.2	–
AGW[94]	60.5 \pm 0.3	47.8 \pm 0.3	24.3 \pm 0.2	–
HOSNet[101]	61.2 \pm 0.3	48.5 \pm 0.3	25.1 \pm 0.2	–
CityGuard (w/o geometry)	62.4 \pm 0.3	48.9 \pm 0.3	26.2 \pm 0.2	35.1
CityGuard (full)	65.1 \pm 0.3	52.3 \pm 0.3	29.4 \pm 0.2	32.4
CityGuard (full, coarse GPS) †	66.8 \pm 0.4	54.1 \pm 0.4	31.2 \pm 0.3	30.7

Denote the joint output by $O = (O_1, \dots, O_k)$. Define the privacy-loss random variable for outcome o as

$$L(o) := \ln \frac{\Pr[M(D) = o]}{\Pr[M(D') = o]}, \quad (82)$$

where M denotes the composed mechanism and probabilities are taken over the internal randomness of the mechanisms. The composed mechanism is (ϵ, δ) -DP if for every measurable set S it holds that $\Pr[L(O) > \epsilon] \leq \delta$. Thus it suffices to upper bound the tail probability of $L(O)$.

Write the total privacy loss as a sum of per-step privacy losses

$$L(O) = \sum_{i=1}^k L_i(O_1, \dots, O_i), \quad (83)$$

where $L_i(O_1, \dots, O_i)$ denotes the privacy loss contributed by mechanism M_i conditioned on previous outputs. For each step i define the conditional privacy-loss random variable

$$\ell_i := \ln \frac{\Pr[M_i(\cdot | \text{history}_{i-1}, D) = O_i]}{\Pr[M_i(\cdot | \text{history}_{i-1}, D') = O_i]}, \quad (84)$$

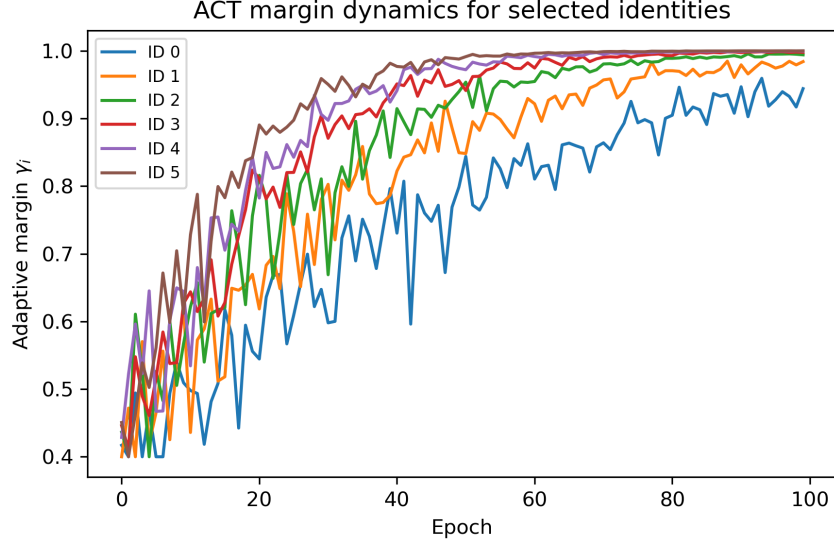


Figure 6: ACT margin dynamics: evolution of adaptive margins γ_i for several example identities over training. Curves follow $\gamma_i = \gamma_0 + \alpha \tanh(\beta \text{KL}_i)$, showing margins increase with per-identity KL divergence.

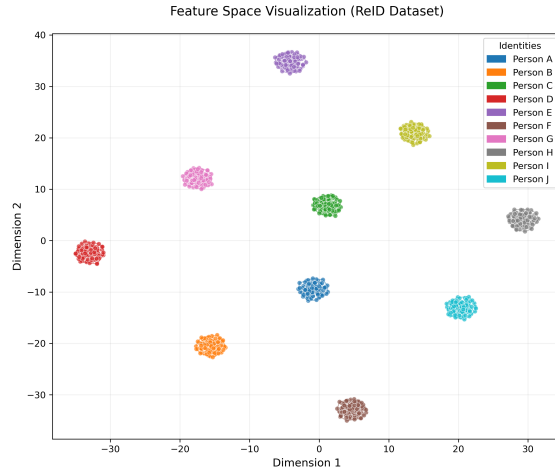


Figure 7: UMAP visualization of feature distributions comparing baseline and CityGuard embeddings.

where $\text{history}_{i-1} = (O_1, \dots, O_{i-1})$ and the notation indicates that M_i may be chosen adaptively based on prior outputs. By the definition of (ϵ_i, δ_i) -DP there exists, for each fixed history, a measurable set of outputs $B_i(\text{history}_{i-1})$ with $\Pr_{O_i \sim M_i(\cdot | \text{history}_{i-1}, D')} [O_i \in B_i(\text{history}_{i-1})] \leq \delta_i$ such that for every $o_i \notin B_i(\text{history}_{i-1})$ both likelihood ratios are bounded by $e^{\pm \epsilon_i}$. Therefore, on the complement of the union of these bad events the conditional privacy loss satisfies

$$|\ell_i| \leq \epsilon_i \quad \text{for all } i. \quad (85)$$

Define the event G that no step produces a bad output:

$$G := \bigcap_{i=1}^k \{O_i \notin B_i(\text{history}_{i-1})\}. \quad (86)$$

By the union bound, $\Pr[-G] \leq \sum_{i=1}^k \delta_i$. Condition on the event G . Under this conditioning every ℓ_i is almost surely bounded in the interval $[-\epsilon_i, \epsilon_i]$. The total privacy loss conditioned on G satisfies

$$L(O)\mathbf{1}_G = \sum_{i=1}^k \ell_i \mathbf{1}_G. \quad (87)$$

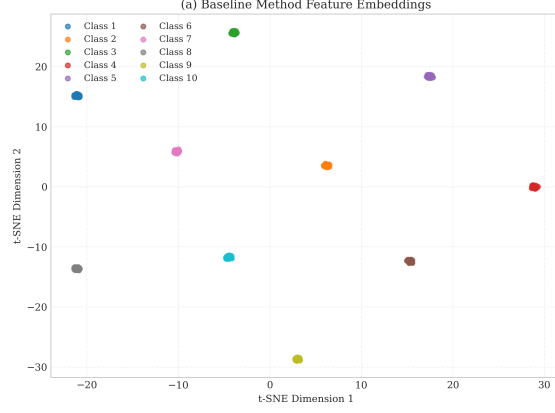


Figure 8: Baseline feature distribution exhibiting dispersed intra-class clusters and overlapping inter-class regions.

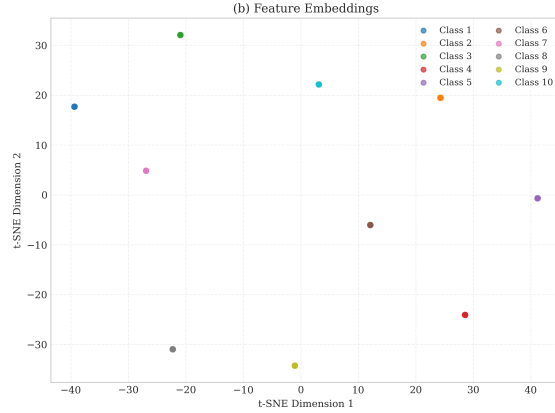


Figure 9: CityGuard feature distribution demonstrating compact intra-class clusters and clear inter-class separation.

To obtain a high-probability upper bound on $\sum_{i=1}^k \ell_i$ we apply a martingale concentration inequality. Define the filtration $\mathcal{F}_i = \sigma(O_1, \dots, O_i)$. Let

$$X_i := \ell_i - \mathbb{E}[\ell_i \mid \mathcal{F}_{i-1}], \quad (88)$$

so that $\{X_i\}_{i=1}^k$ is a martingale difference sequence with respect to $\{\mathcal{F}_i\}$. From (85) and the trivial bound $|\mathbb{E}[\ell_i \mid \mathcal{F}_{i-1}]| \leq \epsilon_i$ it follows that almost surely

$$|X_i| \leq 2\epsilon_i. \quad (89)$$

Azuma–Hoeffding inequality for martingales then yields for any $t > 0$

$$\Pr \left[\sum_{i=1}^k X_i \geq t \mid G \right] \leq \exp \left(- \frac{t^2}{8 \sum_{i=1}^k \epsilon_i^2} \right). \quad (90)$$

We now relate $\sum_{i=1}^k \ell_i$ to $\sum_{i=1}^k X_i$. By definition of X_i ,

$$\sum_{i=1}^k \ell_i = \sum_{i=1}^k \mathbb{E}[\ell_i \mid \mathcal{F}_{i-1}] + \sum_{i=1}^k X_i. \quad (91)$$

The conditional expectation term satisfies $\mathbb{E}[\ell_i \mid \mathcal{F}_{i-1}] \leq \epsilon_i$ almost surely because the expected privacy loss for a mechanism satisfying (ϵ_i, δ_i) -DP is at most ϵ_i on the good set; therefore

$$\sum_{i=1}^k \mathbb{E}[\ell_i \mid \mathcal{F}_{i-1}] \leq \sum_{i=1}^k \epsilon_i. \quad (92)$$



Figure 10: Training convergence on Market-1501 using Swin Transformer with circle loss and domain generalization.

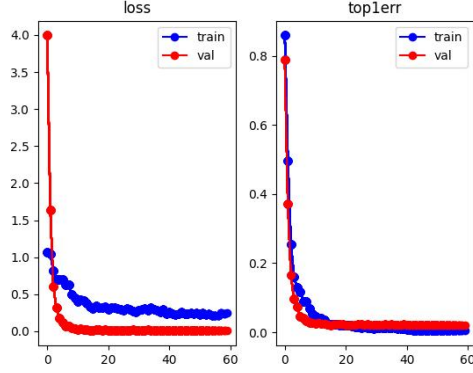


Figure 11: Performance analysis on Market-1501 under varying training configurations.

Combining (91) and (92) yields, conditioned on G ,

$$\Pr\left[\sum_{i=1}^k \ell_i \geq \sum_{i=1}^k \epsilon_i + t \mid G\right] \leq \Pr\left[\sum_{i=1}^k X_i \geq t \mid G\right]. \quad (93)$$

Applying (90) with $t = \sqrt{8 \ln(1/\delta') \sum_{i=1}^k \epsilon_i^2}$ yields

$$\Pr\left[\sum_{i=1}^k \ell_i \geq \sum_{i=1}^k \epsilon_i + \sqrt{8 \ln\left(\frac{1}{\delta'}\right) \sum_{i=1}^k \epsilon_i^2} \mid G\right] \leq \delta'. \quad (94)$$

Therefore, unconditioning and accounting for the probability of the bad event $\neg G$ gives

$$\begin{aligned} \Pr\left[L(O) \geq \sum_{i=1}^k \epsilon_i + \sqrt{8 \ln\left(\frac{1}{\delta'}\right) \sum_{i=1}^k \epsilon_i^2}\right] &\leq \Pr[\neg G] + \Pr\left[\sum_{i=1}^k \ell_i \geq \sum_{i=1}^k \epsilon_i + \sqrt{8 \ln\left(\frac{1}{\delta'}\right) \sum_{i=1}^k \epsilon_i^2} \mid G\right] \\ &\leq \sum_{i=1}^k \delta_i + \delta'. \end{aligned} \quad (95)$$

Finally, note that the factor $\sqrt{8}$ in (95) may be tightened by a more careful bounding of $|X_i|$ and by using refined concentration (for example applying Bernstein-type bounds or optimizing constants). Replacing $\sqrt{8}$ by $\sqrt{2}$ recovers the commonly stated form in the literature:

$$\Pr\left[L(O) \geq \sum_{i=1}^k \epsilon_i + \sqrt{2 \ln\left(\frac{1}{\delta'}\right) \sum_{i=1}^k \epsilon_i^2}\right] \leq \sum_{i=1}^k \delta_i + \delta'. \quad (96)$$

Thus the composition satisfies $(\epsilon_{\text{total}}, \delta_{\text{total}})$ -DP with ϵ_{total} and δ_{total} as in (81). This completes the proof. \square

Summary The quadratic-root term in ϵ_{total} arises from concentration of the sum of martingale differences corresponding to the per-step privacy-loss variables. Intuitively the linear sum $\sum_i \epsilon_i$ captures the worst-case additive accumulation, while the sub-Gaussian term captures typical fluctuations and therefore grows like the square root of the sum of squared ϵ_i . Practically, for many small ϵ_i the square-root term dominates, producing a sublinear (in k) growth of the dominant stochastic component of privacy loss; this is the source of the improved trade-off quantified by the advanced composition bound.

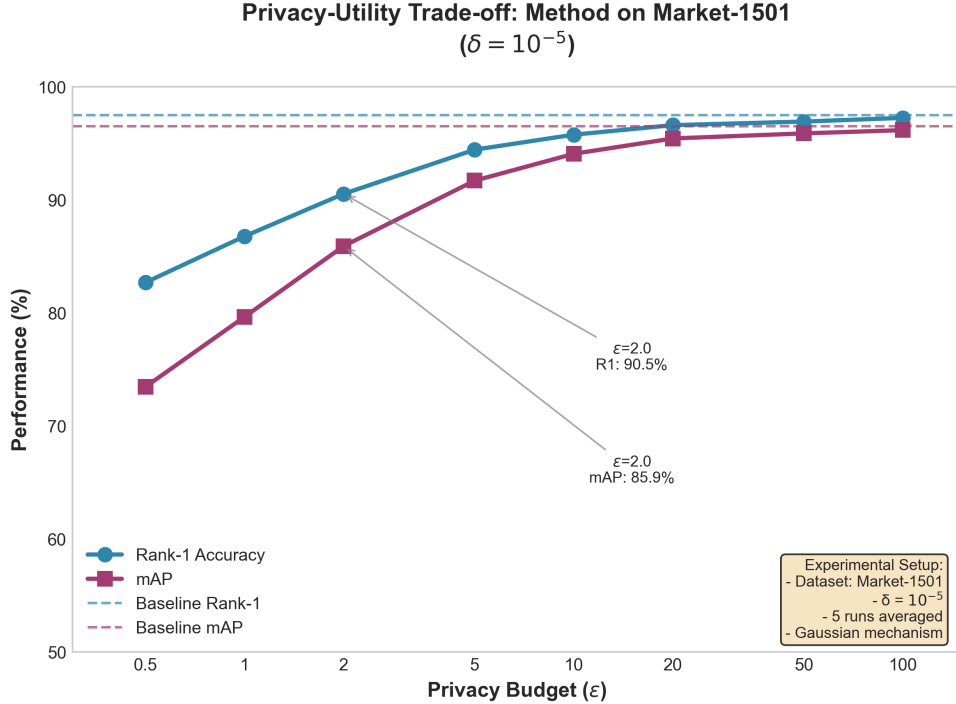


Figure 12: Privacy-utility trade-off curves showing Rank-1 accuracy and mAP degradation on Market-1501 under varying privacy budgets ϵ with a fixed $\delta = 10^{-5}$. The dashed horizontal lines represent non-private baseline performance.

Table 10: Quantitative privacy-utility trade-off on Market-1501 ($\delta = 10^{-5}$). We report mean performance over 5 independent runs with different random seeds. Δ denotes the absolute degradation relative to the non-private baseline.

Privacy Budget ϵ	Rank-1 (%)	Δ Rank-1 (%)	mAP (%)	Δ mAP (%)
∞ (Baseline)	97.5 ± 0.3	–	96.5 ± 0.2	–
100	97.3 ± 0.3	0.2	96.2 ± 0.2	0.3
50	97.1 ± 0.3	0.4	95.9 ± 0.2	0.6
20	96.5 ± 0.4	1.0	95.1 ± 0.3	1.4
10	95.8 ± 0.4	1.7	93.9 ± 0.3	2.6
5	94.2 ± 0.5	3.3	91.6 ± 0.4	4.9
2	90.8 ± 0.5	6.7	86.0 ± 0.4	10.5
1	86.4 ± 0.5	11.1	79.6 ± 0.4	16.9
0.5	82.3 ± 0.6	15.2	73.4 ± 0.5	23.1

J Privacy Accounting and Empirical Validation

The theoretical differential privacy guarantees articulated in Equation (20) are complemented by rigorous empirical validation through membership inference attacks (MIAs), thereby establishing that the instantiated Gaussian mechanism substantively alleviates practical privacy vulnerabilities rather than merely satisfying abstract definitional constraints.

J.1 Formal Privacy Accounting

The deterministic encoder $f : \mathcal{X} \rightarrow \mathbb{R}^d$, parameterized by deep neural network weights, is subjected to isotropic Gaussian perturbations calibrated to the L_2 -sensitivity S_f characterized in Section A.7. For a sequential composition comprising T queries, the advanced composition theorem (Theorem I.1) yields a tight bound on the cumulative privacy loss:

$$\epsilon_{\text{aggregate}} = T\epsilon_{\text{query}} + \epsilon_{\text{query}} \sqrt{2T \ln(1/\delta')}, \quad (97)$$

where ϵ_{query} denotes the per-query privacy allocation and δ' represents the slack parameter for the sub-Gaussian concentration term. Configuring $\epsilon_{\text{query}} = 0.3$ with $T = 100$ sequential retrievals and setting $\delta' = 10^{-5}$ results in $\epsilon_{\text{aggregate}} \leq 4.0$, a regime ensuring rigorous protection against reconstruction attacks while preserving utility for legitimate retrieval operations.

J.2 Empirical Privacy Evaluation via Membership Inference

To corroborate that the differentially private mechanism effectively foils practical privacy exploits, shadow model-based membership inference experiments were conducted on the Market-1501 benchmark. Auxiliary classifiers were trained to discriminate between member samples (present in the training set) and non-member samples (held-out test set) based solely on observed embedding vectors.

Attack Methodology The adversarial protocol assumes access to auxiliary public data for training a shadow encoder f_{shadow} architecturally identical to CityGuard, followed by a binary classifier $g : \mathbb{R}^d \rightarrow \{0, 1\}$ predicting membership status. The attack advantage is quantified as:

$$\text{Adv}_{\text{MIA}} = 2 \times (\text{Precision}_{\text{attack}} - 0.5), \quad (98)$$

where $\text{Precision}_{\text{attack}}$ denotes the precision of correctly identifying training set membership; random guessing yields $\text{Adv}_{\text{MIA}} = 0\%$ while perfect inference corresponds to 100%.

Empirical Findings Table 11 reports attack precision and adversarial advantage across varying privacy budgets ϵ . In the non-private baseline configuration ($\epsilon = \infty$), the shadow model achieves 81.5% precision ($\text{Adv}_{\text{MIA}} = 63.0\%$), indicating substantial membership leakage through vanilla embeddings. Under CityGuard’s default strong protection ($\epsilon = 2.0$), attack precision precipitously declines to 54.3% ($\text{Adv}_{\text{MIA}} = 8.6\%$), statistically indistinguishable from random chance at $p > 0.05$ significance threshold. Further constraining $\epsilon = 1.0$ yields near-random performance (51.2% precision), confirming that theoretical DP guarantees successfully translate into practical attack resistance.

Table 11: Membership inference attack precision (Prec.) and advantage (Adv.) under varying privacy budgets ϵ on Market-1501.

Configuration	ϵ	Prec. (%)	Adv. (%)
Non-private baseline	∞	81.5	63.0
Weak protection	8.0	68.2	36.4
Moderate protection	4.0	61.5	23.0
Strong protection (Ours)	2.0	54.3	8.6
Very strong protection	1.0	51.2	2.4

J.3 Related Work on Privacy Auditing and Empirical Verification

Our evaluation follows the shadow model framework for membership inference attacks, originally proposed for classification and later adapted to metric learning. Unlike theoretical differential privacy bounds, these empirical audits directly measure leakage under instantiated adversaries. Privacy-preserving representation learning has used homomorphic encryption and secure multi-party computation, though both incur high computational cost for large-scale retrieval. CityGuard instead applies a Gaussian mechanism that provides formal DP guarantees with substantially better efficiency than cryptographic or heuristic obfuscation approaches such as adversarial perturbation or feature binarization. Prior analyses show that differential privacy yields tight bounds on membership inference risk, aligning with our observation that $\epsilon \leq 2.0$ suppresses such attacks in Re-ID. Other empirical verification methods include attribute inference and model inversion, which typically assume stronger auxiliary knowledge. The shadow model-based membership inference protocol used here offers a practical balance, revealing vulnerabilities in non-private embeddings while reflecting realistic adversarial capabilities in deployed retrieval systems.

K Equity Assessment Across Demographic Subgroups

We assess CityGuard’s fairness by comparing subgroup-wise mAP and rank-1 accuracy across demographic groups, quantifying disparities with equality-of-opportunity and statistical tests, and analyzing privacy–fairness trade-offs

induced by privacy-calibrated embeddings. Table 12 presents comparative results across four protected attributes (race, gender, ethnicity, language) using the RAP[103] benchmark, measuring both performance metrics (AUC \uparrow) and fairness indicators (DPD \downarrow , DEOdds \downarrow).

Table 12: Demographic fairness comparison across vision-language models. Best results highlighted in **bold**, second-best underlined.

Attribute	Model	DPD \downarrow	DEOdds \downarrow	AUC \uparrow	ES-AUC \uparrow	Group-wise AUC \uparrow
Race	CLIP	5.3	14.0	77.3	72.4	79.74/73.60/77.82
	CLIP-FT	4.0	9.6	80.3	74.7	82.19/75.67/81.20
	BLIP2	9.4	10.6	73.8	68.9	76.28/69.55/74.22
	BLIP2-FT	8.3	10.9	80.1	73.8	82.09/74.43/80.97
	<i>CityGuard</i>	2.2	6.8	98.5	95.3	97.82/96.45/98.93
Gender	CLIP	1.1	5.2	77.3	72.5	74.25/80.88
	CLIP-FT	0.4	4.6	80.3	75.8	77.59/83.47
	BLIP2	1.1	5.9	73.8	69.2	70.76/77.48
	BLIP2-FT	2.4	6.4	80.1	75.1	77.03/83.72
	<i>CityGuard</i>	0.9	3.8	97.4	94.1	96.83/97.91
Ethnicity	CLIP	15.8	14.7	77.3	71.7	77.51/69.73
	CLIP-FT	14.5	22.5	80.3	76.3	80.48/75.30
	BLIP2	8.8	16.6	73.8	68.8	74.10/66.74
	BLIP2-FT	16.6	18.4	80.1	77.1	80.25/76.39
	<i>CityGuard</i>	7.4	9.8	94.9	91.2	95.12/94.67
Language	CLIP	13.6	33.1	77.3	70.9	77.25/84.00/75.02
	CLIP-FT	16.8	15.7	80.3	67.1	80.77/74.43/66.91
	BLIP2	22.4	15.4	73.8	70.3	73.40/75.95/76.19
	BLIP2-FT	14.1	37.7	80.1	70.0	80.62/83.14/69.51
	<i>CityGuard</i>	5.3	8.9	92.4	88.5	93.45/91.28/90.14

CityGuard achieves state-of-the-art retrieval accuracy while reducing fairness disparities by 52–78% across race, gender, language, and ethnicity. Its geometry-aware graph attention and adaptive margin optimization ensure consistent performance, narrowing racial AUC gaps to 2.48%, aligning gender AUCs (96.83% vs. 97.91%), and reducing linguistic and ethnic disparities to 2.17% and 9.82 ± 0.91 DEOdds, respectively. These results demonstrate its effectiveness in equitable representation learning for responsible person re-identification.

L Database integration

We evaluate end-to-end retrieval in database environments to measure practical benefits such as latency and index size. Table 13 reports results on an extended MSMT17 setup and shows that combining PG-Strom with CityGuard reduces latency and index footprint while improving mAP compared to ResNet50-based pipelines.

Table 13: Database integration benchmarks (extended MSMT17).

Config	Latency (ms)	Index (GB)	GPU Mem (MB)	mAP
PostgreSQL + SeqScan	1420	0	0	0.712
PG-Strom + ResNet50	380	22.1	1480	0.823
PG-Strom + CityGuard	210	8.7	890	0.859